Induced Seismicity in the Bergermeer Field: Hypocenter Relocation and Interpretation

Q-con GmbH

Geothermal reservoir engineering

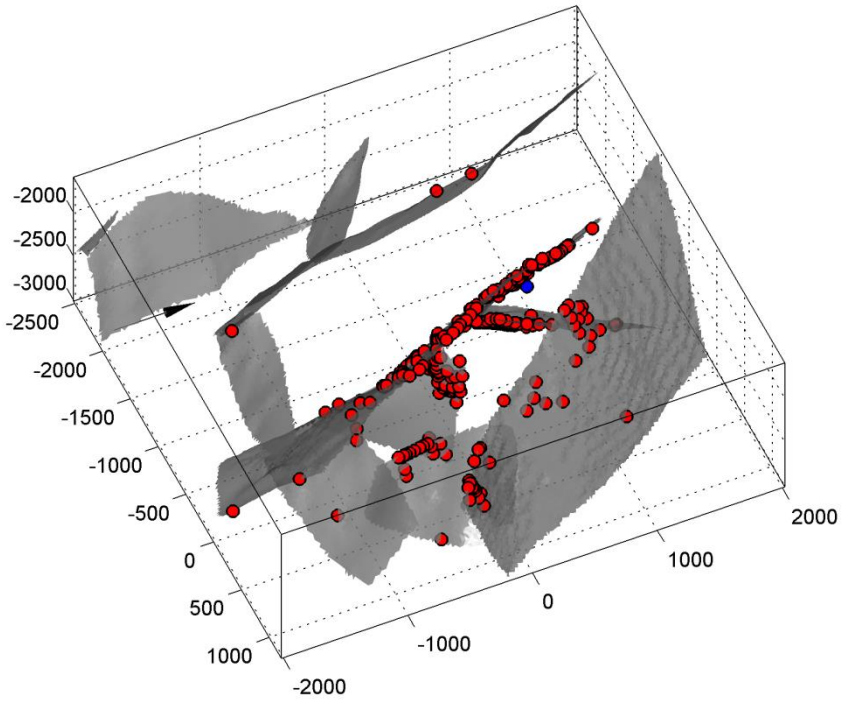

TAQA003

Report title:	Induced Seismicity in the Bergermeer Field: Hypocenter Relocation and Interpretation
Authors:	Stefan Baisch; Christopher Koch; Robert Vörös; Elmar Rothert
Report date:	12. February 2016
Project:	Bergermeer
Prepared for:	Taqa Energy B.V.
Version:	DRAFT
Archive No.:	TAQA003

Contents

Contents

1 SUMMARY

In a previous study (TAQA002) we assessed the quality of the Bergermeer earthquake data catalogue compiled by different service providers for the time period January 2010 to July 2015. Our assessment revealed that earthquake data required re-processing because the existing earthquake catalogue is based on inaccurate or false tool orientations, does not provide event-specific hypocenter location uncertainties, and does not explicitly account for non-unique (symmetric) solutions.

The current report documents the re-processing and interpretation of the seismic events. The main results can be summarized as follows:

- Tool orientations were determined for all different monitoring phases except for phase 1, for which no checkshot data was available. Consequently, no hypocenters could be determined for the 4 earthquakes occurring during phase 1.
- Using a calibrated velocity model for the reservoir rocks, absolute hypocenter locations were determined for 323 events occurring near or within the reservoir. Regional events (i.e. events not associated with the Bergermeer reservoir) were excluded from the analysis.
- Event specific hypocenter location errors were determined including systematic error contributions from the assumed seismic velocity model and the receiver orientations. On the 2σ confidence level, total hypocenter location errors range between a few ten meters to the kilometer scale. Typical (median) location errors are 250 m in the two horizontal directions and 375 m vertically.
- A total number of 104 non-unique hypocenter solutions ('symmetrical solutions') were obtained. For these, the observed moveout of the P-phase onset is too small to unambiguously discriminate between the two possible solutions.
- The earthquake catalogue was clustered based on seismogram similarity. Events belonging to the same cluster family have closely spaced hypocenters. Cluster families enabled us to identify the 'true' hypocenter location for 30 events out of the 104 symmetrical solutions. For the remaining 74 events, the two alternative ('symmetrical') hypocenter locations were kept in the catalogue.
- Based on waveform similarity, relative hypocenter locations with respect to a master event were determined for cluster events. Inter-event distances are typically in the order of a few tens of meters.
- Event magnitudes were determined using the definition of Hanks & Kanamori (1979). The magnitude of the strongest event is M_w=0.9. Compared to the previous catalogue, this magnitude has increased by 0.2 units (M_w). The difference results from larger source-receiver distances after re-locating the earthquake.
- Considering uncertainties associated with catalogue completeness and the viewing bias, the magnitude of the strongest event is within the 2σ confidence bounds of the magnitude-frequency distribution, although at the upper limit.
- Within their hypocenter location uncertainties, almost all events can be shifted to one of the mapped reservoir faults ('fault collapsing'). The associated statistics of the movement

vectors is approximately consistent with expectations when assuming that events are truly originating on the faults.

- Observed seismic activity is strongly clustered in space and time. Stress criticality on faults as evidenced by seismic activity has a transient signature. Fault patches that were seismically active during refill can become silent after a certain point in time. On the central fault, where most seismicity occurs, and on the eastern fault we observe a North-South migration of the seismicity with time.
- We propose a conceptual model, where seismicity during refill occurs on the main faults at those locations, which were already seismically active during production. Within this model the transient occurrence of observed seismic activity during refill can be used to constrain stress paths and thus for calibrating a numerical model.

Recommendations for future work:

- The spatio-temporal distribution of seismicity exhibits some systematic characteristics which might be an indicator for a comparatively small seismic hazard during refill. Most notably, regions of seismic activity becoming silent at a certain point in time (despite continued refill) could indicate that stress paths in a particular region move away from criticality. In a similar way, the period of low seismic activity between September 2012 and January 2014 could be attributed to changing the injection pattern (compare Figure 21). Concerns, however, remain that the drop in seismicity rates might simply be an artifact from changing acquisition parameters (chapter 6), since periods of low activity approximately correlate with specific monitoring phases. To ensure that the observed drop in seismic activity has a physical origin, we recommend reviewing the trigger settings and/or applying a consistent trigger to the entire data set.

2 TOOL ORIENTATION

Based on the checkshot data summarized in TAQA002 (Table 3), tool orientations were determined for all monitoring phases.

The orientation procedure comprises the following steps:

1. Seismograms recorded in the instrument system (left-handed) were rotated into the wellbore trajectory system (i.e. vertical instrument axis is parallel to wellbore trajectory).

2. A second rotation around the vertical instrument axis is performed to determine the best match between the observed signal beam and the theoretical beam direction. The mismatch is taken as a direct measure for the systematic bias resulting from sensor orientation uncertainties.

Signal beam directions were determined using optimized windows on which the Jurkevics rectilinearity (Jurkevics, 1988) is simultaneously maximized (compare TAQA002).

Resulting sensor orientations are documented in Appendix A. Sensor orientations could not be determined for phase 1, for which no checkshot data is available, and for geophone level 1 in phase 3 due to a low signal-to-noise ratio. All other tool orientations yield consistent results, where the mismatch between observed and theoretical beam directions typically is in the order of 10 degrees.

3 ABSOLUTE HYPOCENTER LOCATIONS

We used the calibrated, homogeneous velocity model (Table 4 in TAQA002, model 'selected checkshots') to determine absolute hypocenter locations based on observed S-P traveltime differences and observed directions of incoming P-waves.

Following the approach sketched in TAQA002, we determined the direction of the incoming P-wave signals in 16 time windows with varying length between 0.5 T and 2 T, where T refers to the signal period. We computed the weighted mean from the resulting 16 estimates for azimuth and inclination. Weights are defined as the square of the Jurkevics rectilinearity.

Hypocenters were determined by a linearized inversion (e.g. Bulut et al., 2009) allowing the determination of formal location errors by projecting observation residuals into the model space (e.g. Baisch et al., 2002). Total hypocenter location errors were determined considering all contributions listed in Table 6 of TAQA002.

On the 2σ confidence level, total hypocenter location errors range between a few ten meters to the kilometer scale. Typical (median) location errors are 250 m in the two horizontal directions and 375 m vertically (Figure 1).

It should be noted, however, that the assumed seismic velocity model becomes less accurate for earthquakes occurring in the under- or overburden. This could introduce another, yet unmodelled, error contribution for events located significantly above or below the reservoir. We excluded events with distances > 3 km ('external events' occurring outside the reservoir) from our analysis.

Figure 2 shows the resulting hypocenter locations. Due to the specific event-receiver geometry, hypocenter locations for 104 events are non-unique. I.e. a 'symmetric' hypocenter exists, which cannot be distinguished from the true hypocenter due to an extremely small P-wave moveout.

Figure 3 and Figure 4 compare hypocenter locations before and after re-processing of the catalogue. We note a considerable number of events for which hypocenters have shifted significantly. Scaling of the hypocentral shifts by the event specific confidence limits determined in the current study yields 30% (19%) of the events being shifted by more than 1σ (2σ) after re-processing.

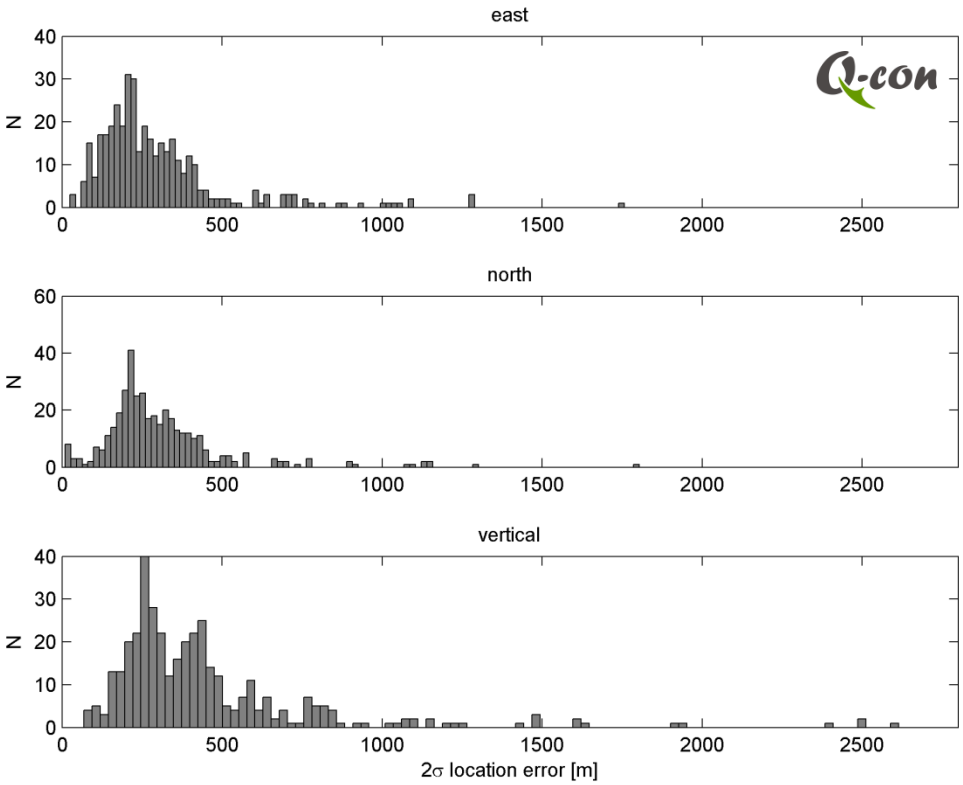

Figure 1: Histograms showing 2σ total hypocenter location uncertainties into eastern (top), northern (middle) and vertical (bottom) directions.

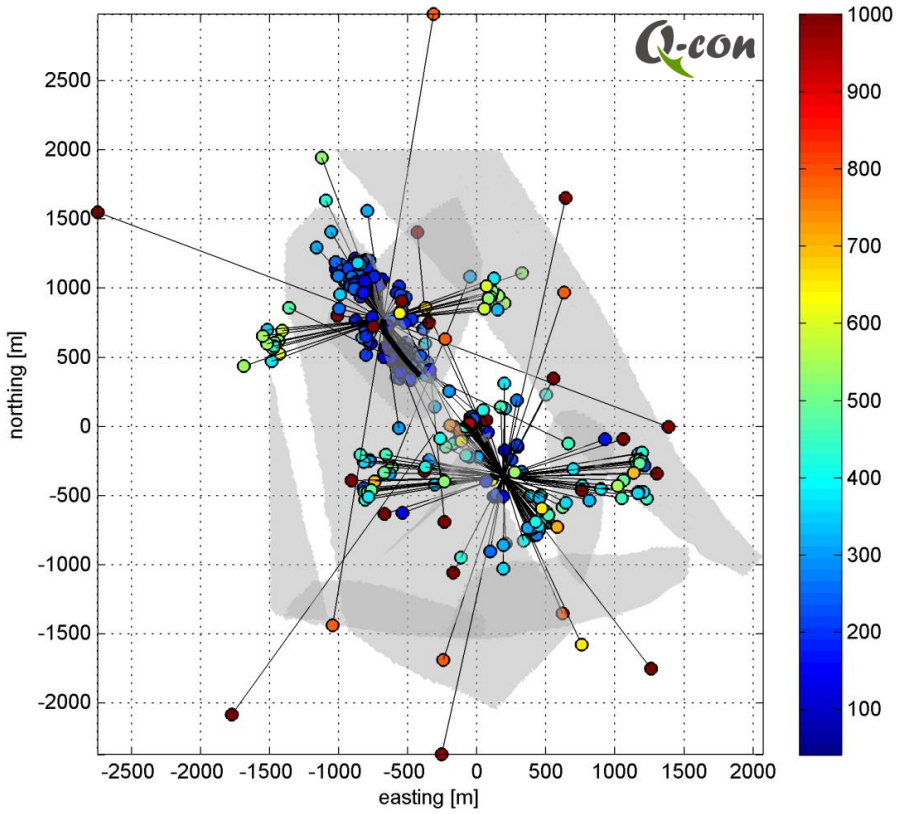

Figure 2: Hypocenter locations in map view. Color encoding denotes the 2σ hypocenter location error averaged over the three spatial components. The colorbar is saturated at 1,000 m. Non-unique ('symmetric') hypocenter locations are connected by lines. Grey shading indicates mapped faults.

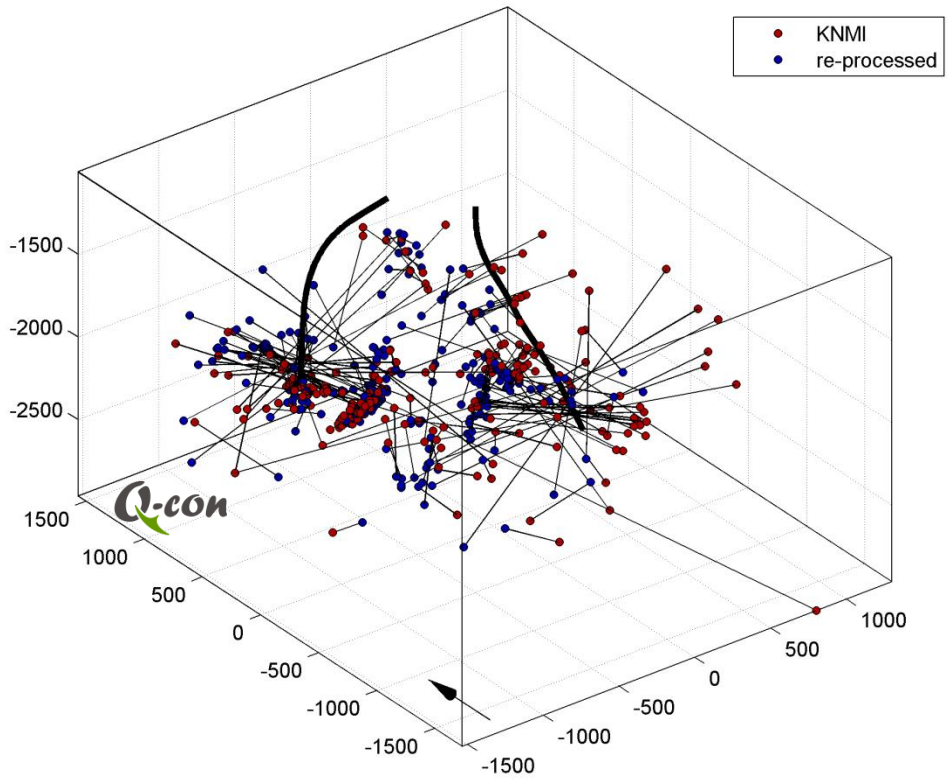

Figure 3: Hypocenter locations before (red) and after re-processing (blue). Associated events are connected by black lines.

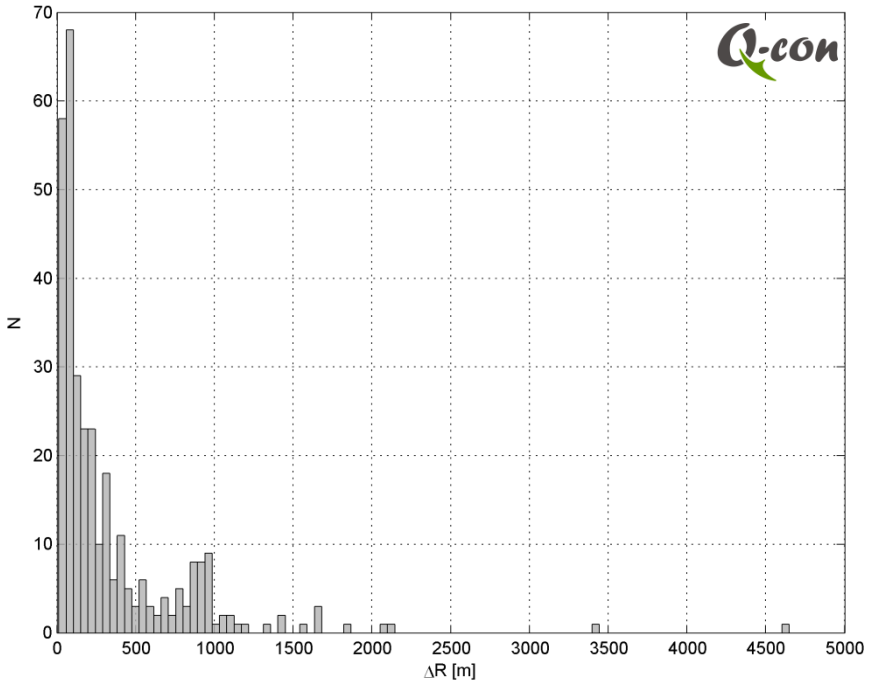

Figure 4: Relative distance between hypocenters before and after relocation. For those events which have two symmetric hypocenter solutions, the solution which is closer to the original hypocenter has been considered.

4 CLUSTERING AND RELATIVE HYPOCENTER LOCATIONS

The earthquake catalogue was clustered based on seismogram similarity determined at 3 different geophone levels. Figure 5 shows the waveform similarity matrix for 323 located reservoir events recorded at downhole geophone level 2 (channel 2). Event ordering is arranged such that event pairs with high waveform similarity tend to align along the main diagonal. The color scale is saturated towards low similarities to enhance cluster families showing up in warm colors. From this diagram we identify event families exhibiting extremely similar waveforms (see example in Figure 6). Hypocenters of these events are closely spaced (e.g. Baisch et al., 2008) thus providing additional information for discriminating between true and symmetrical hypocenter solutions (compare previous section):

If at least one member of a cluster family exhibits a unique hypocenter solution, symmetrical hypocenter solutions can be discarded for other members of the same cluster. Clustering enabled us to discriminate between true and symmetrical solution for 30 events. For these events, relative hypocenter locations with respect to a master event (i.e. an event from the same cluster which has a unique hypocenter solution) were determined. Relative travel-time differences between master and slave events were determined based on waveform similarity following Poupinet et al. (1984). Similarly, relative signal azimuth and incidence angles were determined by maximizing waveform similarity. The resulting inter-event distances pairs are typically in the order of a few tens of meters.

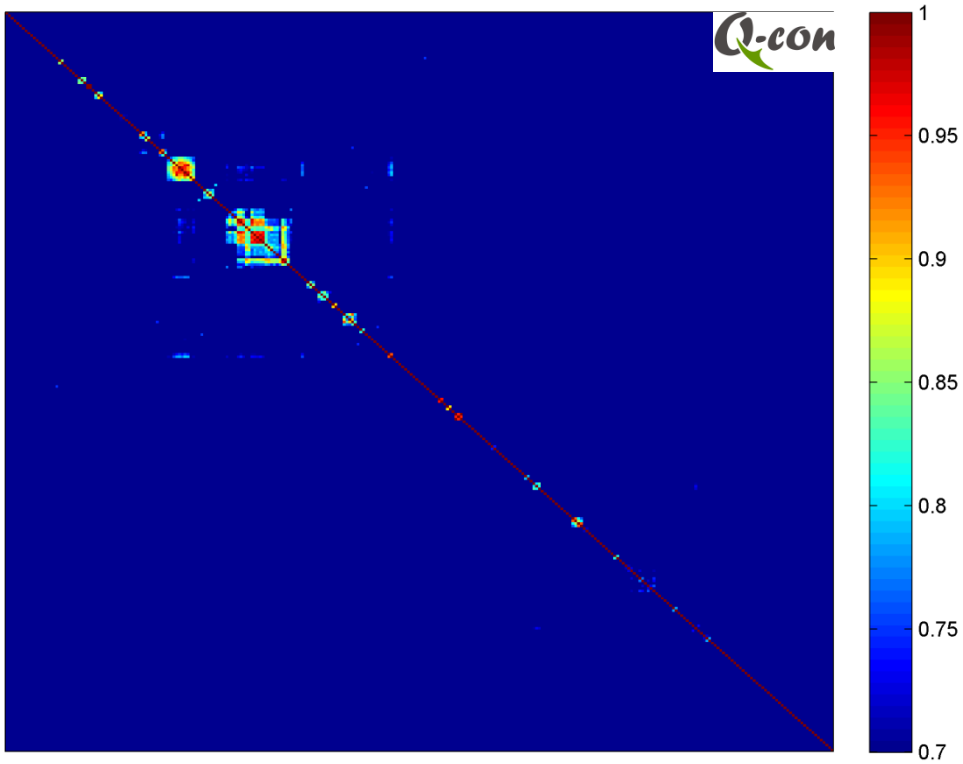

Figure 5: Similarity matrix for 323 located reservoir events. Color encoding denotes waveform similarity (cross correlation) between event pairs. Event ordering is arranged such that clusters with larger similarity tend to align along the main diagonal.

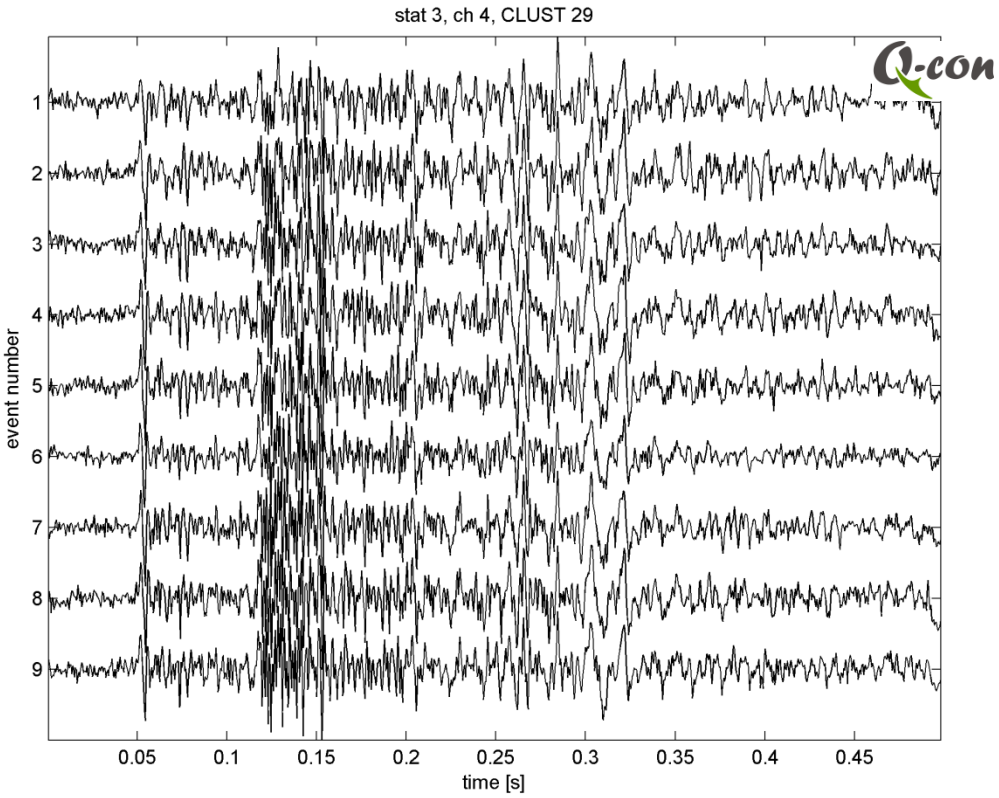

Figure 6: Waveform section of 9 events belonging to a cluster family recorded at channel 1 of downhole geophone level 1. Events are aligned according to their waveform similarity following the approach of Baisch et al. (2008).

5 FAULT COLLAPSING

We investigated the hypothesis that all events occurred on mapped faults. For this, we moved individual hypocenters component-wise within their 2σ confidence limits to the closest patch of a mapped fault ('fault collapsing'). By this, we approximate the error-ellipsoid by a box with sidelength defined by the 2σ error limits in the three Cartesian directions.

Only four hypocenter solutions (corresponding to 1% of the data) do not match any of the mapped faults within their component-wise 2σ confidence limits (Figure 7, Figure 8). Three of these have a symmetric hypocenter solution which matches a fault. For the fault-collapsed catalogue (Appendix D), we interpret the symmetric solution of these three events to be the 'true solution'. After discarding the alternative solution for the three events in the fault-collapsed data catalogue, only a single event remains which cannot be associated with one of the mapped faults.

To this end, 'fault collapsing' is an *ad hoc* approach for testing whether or not the above hypothesis is consistent with the data. The fault collapsed catalogue does not necessarily reflect actual hypocenter locations, since an infinite number of alternative catalogues exists, where hypocenters were shifted within their confidence limits.

Additional information, however, is contained in the statistics of the movement vectors (compare the original collapsing method by Jones & Stewart, 1997). If fault collapsing moves all hypocenters to their true locations, then the statistics of the movement vectors should follow a chi-square distribution with 3 degrees of freedom.

Due to the elongated structure of the mapped faults, however, 'fault collapsing' does not necessarily move a hypocenter to its true location on the fault (compare sketch in Figure 9). Mapped faults strike approximately North-South and are steeply dipping. Therefore, the unmodelled contribution Δr of the movement vectors dominates in North-South and vertical directions. This is the reason why we have chosen a component-wise approach.

Figure 10 shows the statistics of the movement vectors. In East-Western direction, the statistics is approximately consistent with values expected from a normal distribution. In the two other directions (where Δr dominates), hypocenters can be moved much 'quicker' onto a fault, which could be explained by considering unmodelled Δr contributions. Thus hypocenter locations and movement vectors are approximately consistent with the hypothesis that all seismicity occurred on one of the mapped faults.

We note, however, that the nearest fault-collapsed catalogue represents a data interpretation. In Appendix B and Appendix C we confirmed that the structural complexity associated with this model is not an artifact of noisy data. Reducing the number of seismically active faults to a minimum (minimum complexity model, Appendix B) and a maximum (maximum complexity model, Appendix C) yields similar structural complexity.

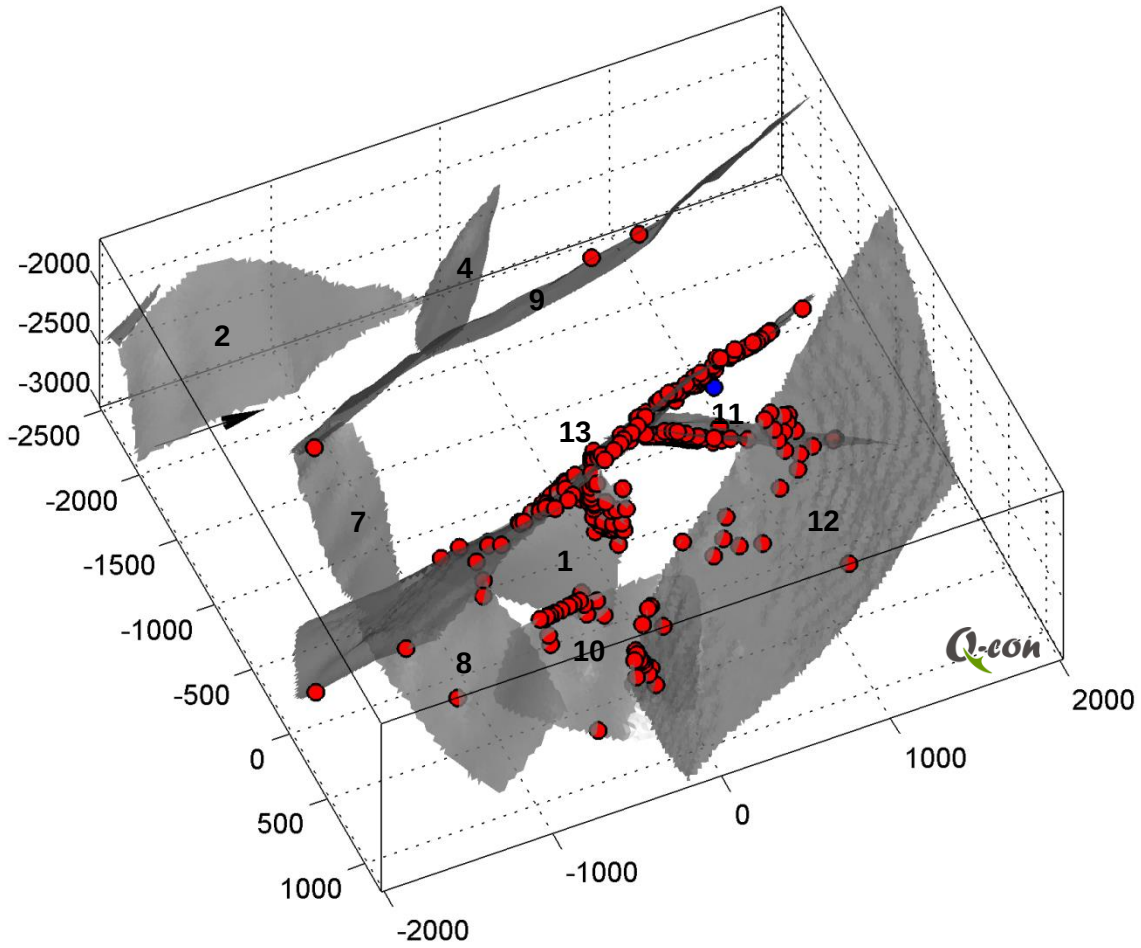

Figure 7: Nearest fault-collapsed hypocenter locations of all reservoir events. Faults are displayed in grey and assigned index numbers for reference (see also Appendix E). Hypocenters that can be shifted onto a fault within their confidence limits show up in red. Four hypocenter solutions do not match a mapped fault within their confidence limits. Three of these have symmetric solutions and were discarded; the remaining event was assigned its original hypocenter (blue dot).

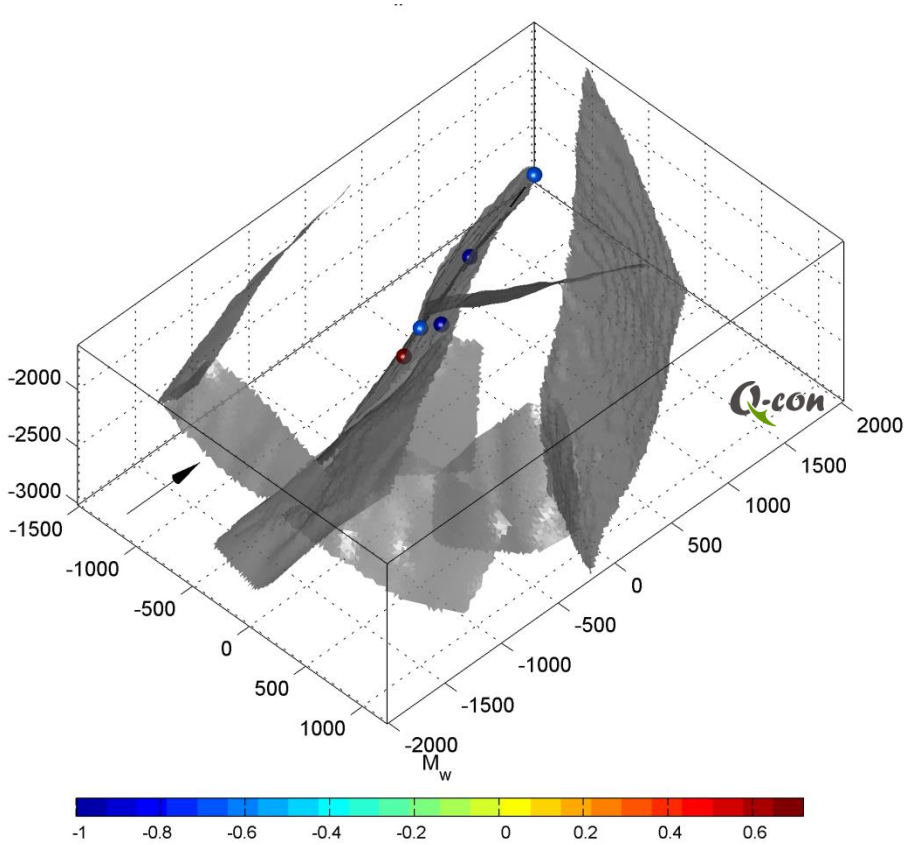

Figure 8: Fault-collapsed hypocenter locations of the strongest four events with M_w>-1.0. Color encoding denotes event magnitude (saturated at M_w=0.7).The hypocenter location of one of the four events is not unique. Both hypocenter solutions are shown and are connected by a straight line. Both solutions match the same fault.

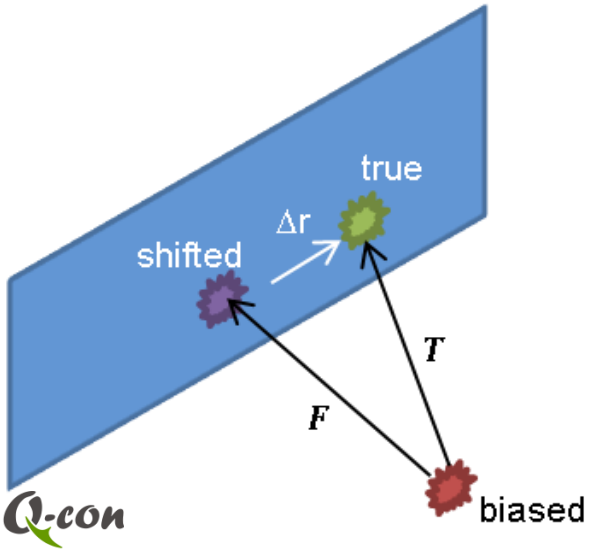

*Figure 9: Sketch illustrating fault-collapsing. Hypocenters ('biased location') are shifted by vector **F** within their confidence limits towards the closest patch of the nearest fault ('shifted location'). The 'true hypocenter location' may be on the fault but at a different position separated by vector **Δr= T - F**.*

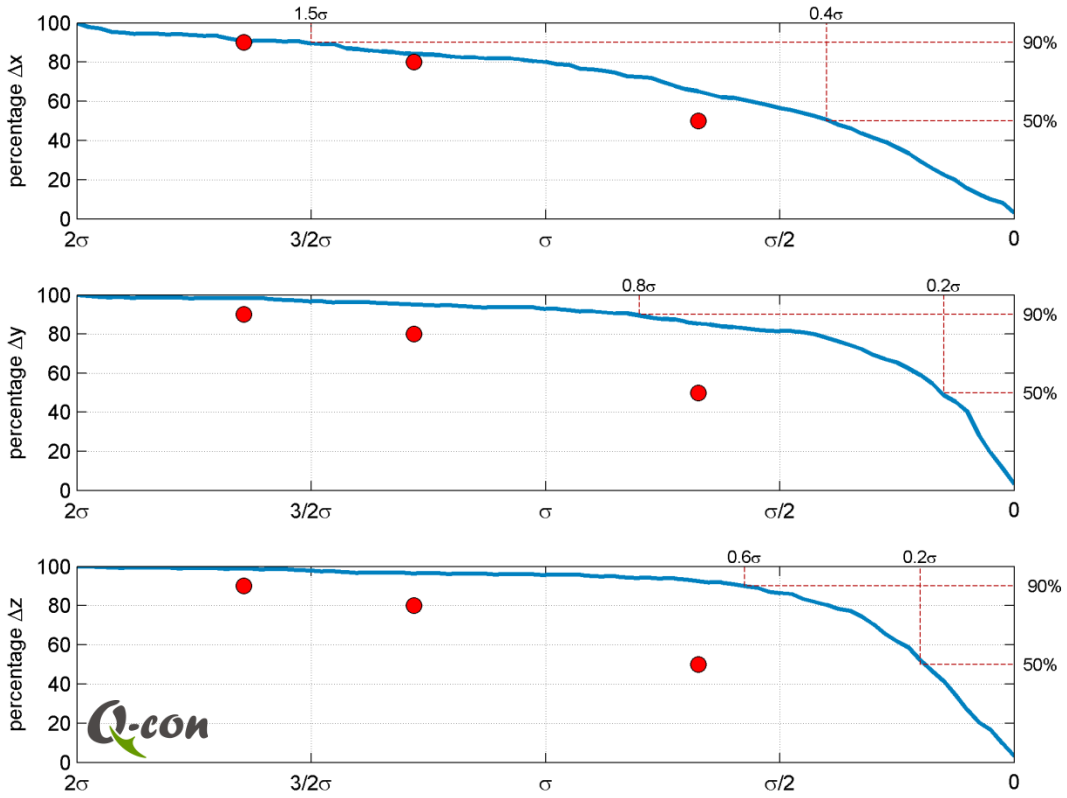

Figure 10: Hypocenter movement statistics after fault-collapsing in eastern (top), northern (middle) and vertical (bottom) direction. Hypocenter movements are scaled to location uncertainties (σ). Red dots indicate expected values assuming that location errors are normally distributed in each spatial direction. See text for details.

6 EVENT MAGNITUDE

We determined Hanks & Kanamori (1979) moment magnitudes for all reservoir events following the approach outlined in TAQA002 (chapter 7).

Due to changes of hypocenter locations after re-processing, event magnitudes slightly changed compared to the previous catalogue. Most notably, the strongest reservoir event now has a magnitude of M_w=0.9 instead of M_w=0.7 in the previous catalogue. Figure 11 shows the temporal evolution of event magnitudes.

We note a systematic decrease of seismic activity with the beginning of monitoring period 6 (BGM03a) in September 2012 lasting until January 2014 (beginning of monitoring phase 9 in BGM05). The period of low seismicity activity does not correlate with moving the geophone string from BGM03a to BGM05, thus indicating a physical cause. We can, however, not exclude that the period of low seismic activity may be an artifact from changing acquisition parameters (trigger settings), which were not quality controlled within the current study.

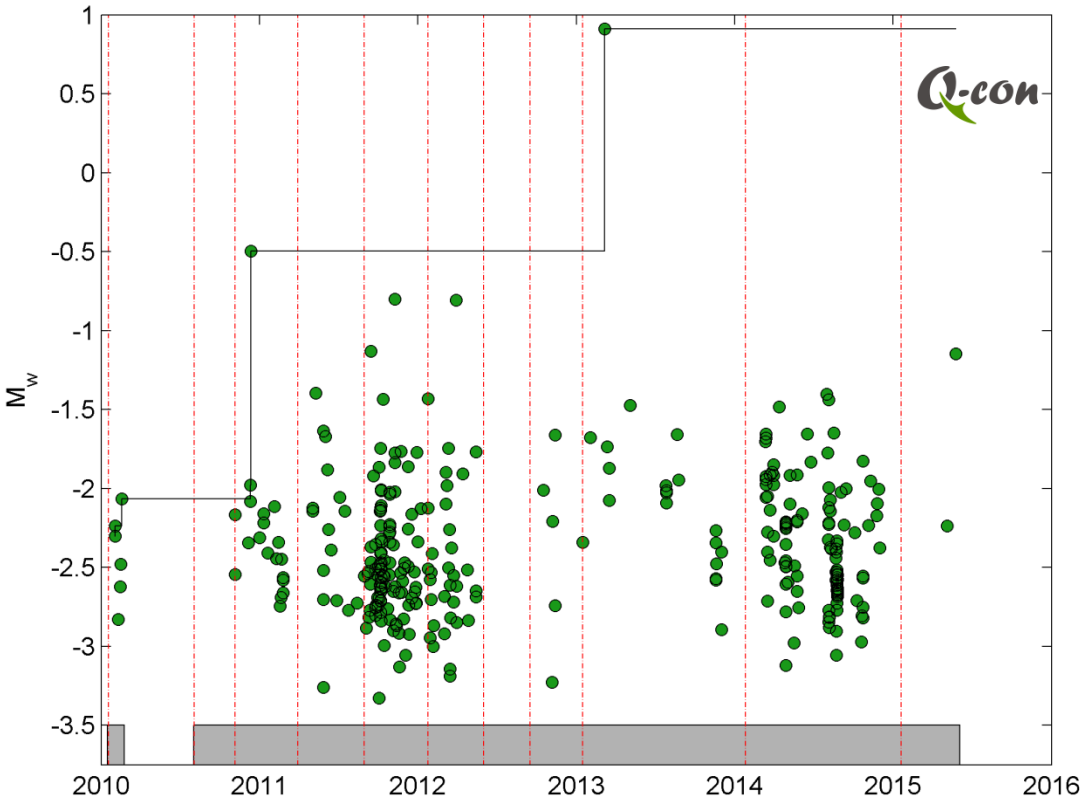

Figure 11: Temporal evolution of seismic event magnitudes (dots). Grey bar at the bottom indicates time intervals during which seismic monitoring was performed. Smaller downtimes up to several days are not shown (these can be found in Appendix A of TAQA002). Different monitoring periods are indicated by red vertical lines. Stair function denotes the temporal evolution of the maximum magnitude.

6.1 Catalogue Completeness and Viewing Bias

Statistical analysis of the occurrence probability of an event with a certain magnitude requires knowledge of the magnitude of completeness M_c of the catalogue, i.e. above which magnitude level the catalogue can be considered complete. Frequently, the magnitude of completeness is estimated from observation data as the magnitude below which observations start deviating from a Gutenberg-Richter type distribution (Wiemer and Wyss, 2000).

For the current data set, this approach is limited by two factors:

1. missing data, i.e. seismic monitoring was not performed continuously and instrument downtimes on average are in the order of 12% (compare Appendix A in TAQA002),
2. the viewing bias, i.e. the smallest magnitude events can only be detected if they occur close to the geophones (thus M_c depends on hypocentral distance[1]).

During instrument downtimes, events can only be detected if they are strong enough to be recorded by the permanent KNMI monitoring network. At Bergermeer, the detection threshold of the official KNMI network is in the order of approximately M_w=1 (Dost et al., 2012). Several additional (near-surface / surface) stations in the vicinity of the Bergermeer field are operated by KNMI. Details of these stations were not available for the current study but we estimate that the local stations may detect reservoir seismicity as small as $M_w \approx 0$. This implies that the magnitude of completeness during downtimes of the geophone array is at $M_w \approx 0$.

If seismicity follows a stationary process, the impact of missing data on b-value analysis (section 6.2) tends to average out for long observation intervals, provided that data gaps occur randomly in time. Analyses of the total event productivity (a-value) or cumulative seismic energy, however, can be significantly affected by missing data.

Based on seismic noise recordings from the downhole geophones we estimate the viewing bias following the approach of Eaton et al. (2014). We distinguish between the viewing bias associated with event detection and the viewing bias resulting from the additional requirement that P- and S-phase onsets can be clearly identified for hypocenter determination (Figure 12). Averaged noise conditions turned out to be very similar for all deployment periods justifying the use of the same viewing bias functions for all monitoring periods.

Figure 13 to Figure 15 show the lateral extension of the viewing bias in comparison to recorded event magnitudes. As expected, many of the smallest (catalogued) events occur close to monitoring wells. For example, moving the geophone array from BGM3a to BGM5 illuminates a cluster of small magnitude seismicity south-east of BGM5, which was previously not seen from BGM3a. Importantly, however, not all of the small magnitude event clusters are centered at the observation wells, demonstrating that the spatial seismicity distribution

[1] hypocentral distance is defined as the distance between the centroid of the downhole geophones and the hypocenter

reflects physical processes rather than the positioning of the monitoring instruments.

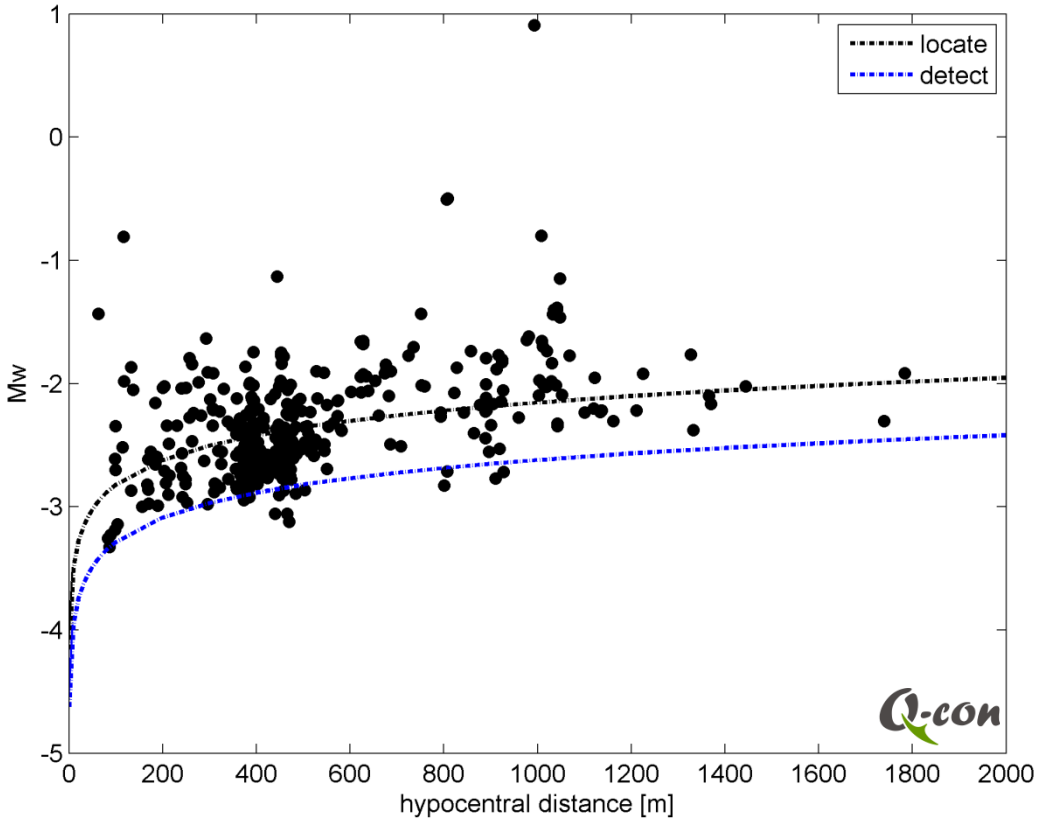

Figure 12: Event magnitude as a function of hypocentral distance for all located reservoir events. Dashed lines show the viewing bias determined by the approach of Eaton et al. (2014), distinguishing between the signal strength required for detecting an event (blue) and for locating an event (black).

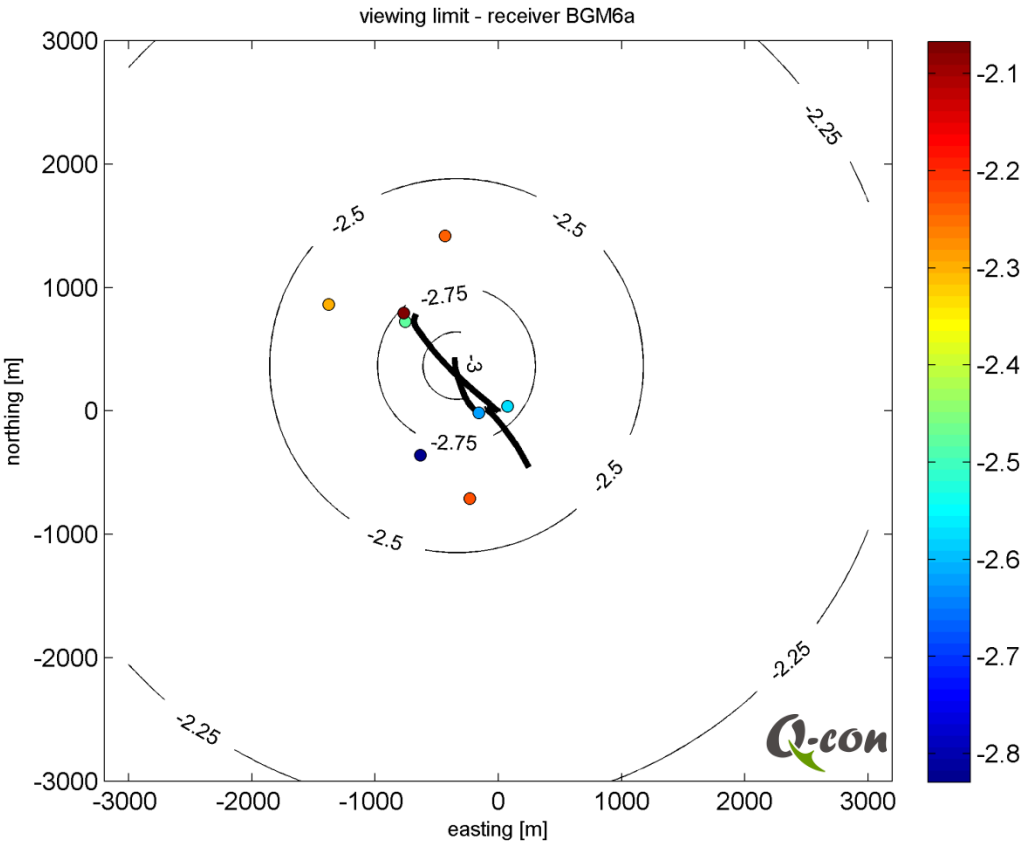

Figure 13: Lateral viewing bias for event detection with geophones deployed in BGM6a. Contour lines denote the viewing bias for events occurring at the depth level of the geophone array. Colored dots denote epicenters of events occurring during the associated monitoring phase with color encoding indicating event magnitude. Black line shows surface projection of well trajectories BGM3a, BGM5, and BGM6a.

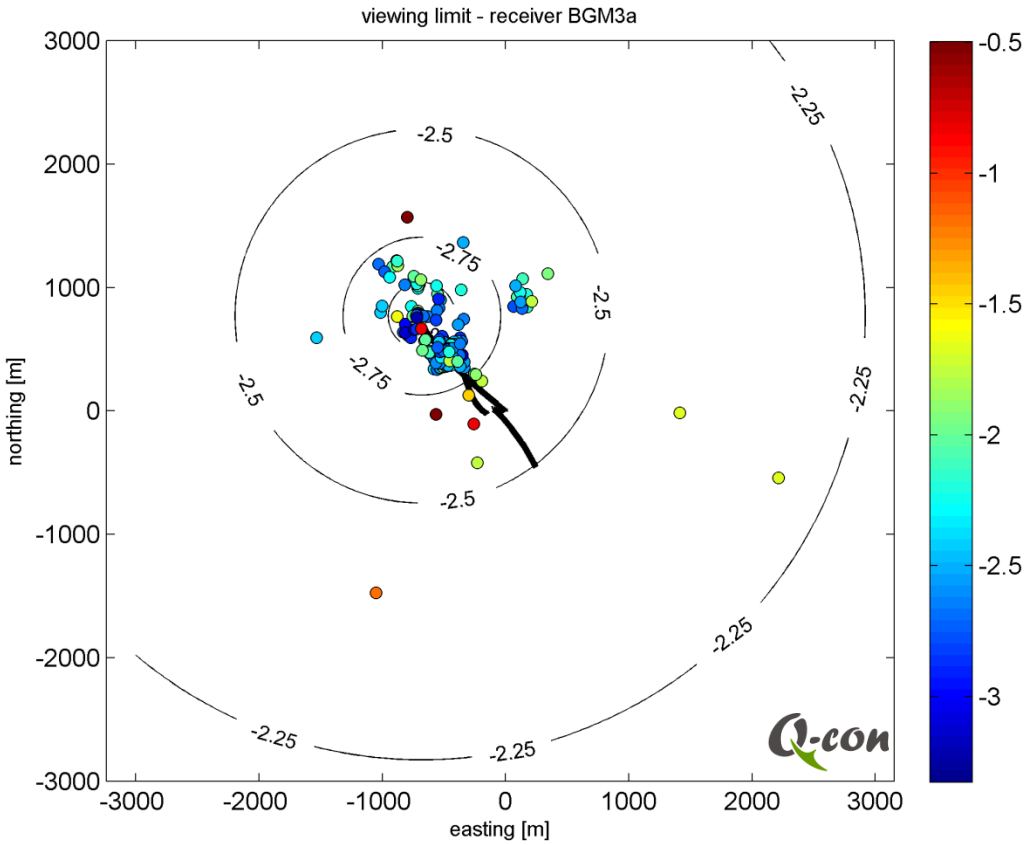

Figure 14: Lateral viewing bias for event detection with geophones deployed in BGM3a. Contour lines denote the viewing bias for events occurring at the depth level of the geophone array. Colored dots denote epicenters of events occurring during the associated monitoring phase with color encoding indicating event magnitude. Black line shows surface projection of well trajectories BGM3a, BGM5, and BGM6a.

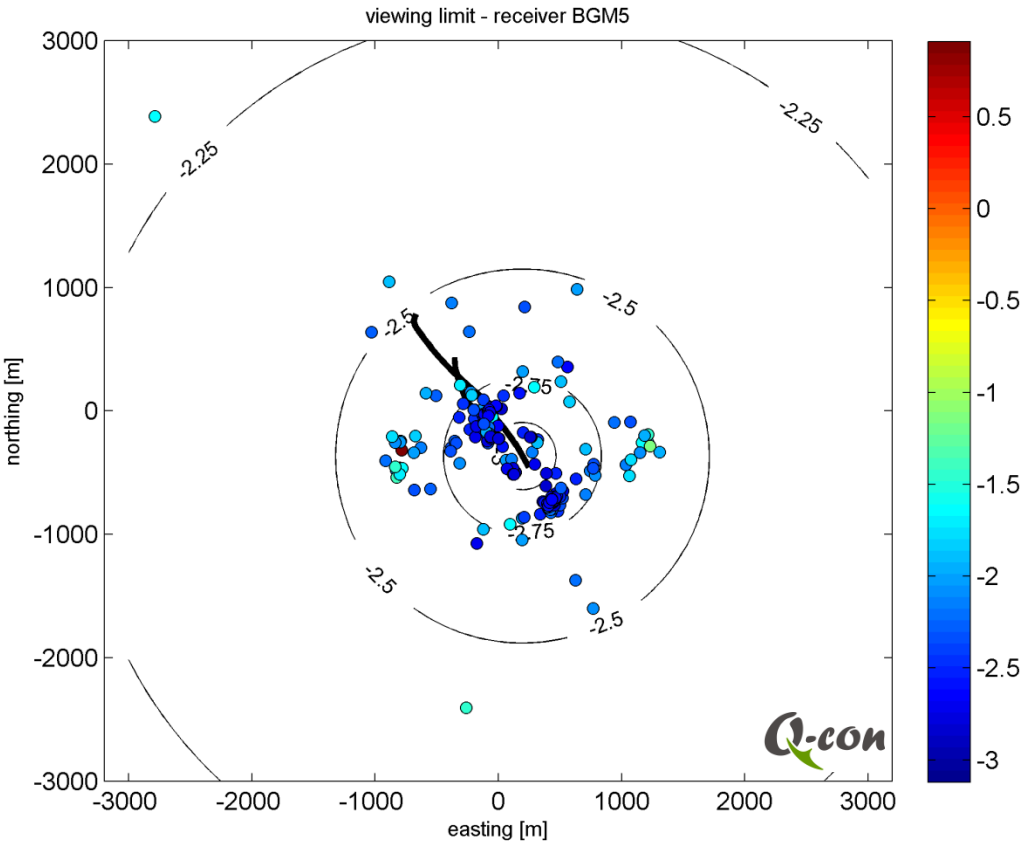

Figure 15: Lateral viewing bias for event detection with geophones deployed in BGM5. Contour lines denote the viewing bias for events occurring at the depth level of the geophone array. Colored dots denote epicenters of events occurring during the associated monitoring phase with color encoding indicating event magnitude. Black line shows surface projection of well trajectories BGM3a, BGM5, and BGM6a.

6.2 Magnitude Frequency Distribution

Figure 16 shows the magnitude frequency distribution for the entire set of catalogued reservoir events. Shaded area denotes the 95% confidence region determined from the Poisson counting error (e.g. Bourne et al., 2014).

From this diagram it appears that the largest M_w=0.9 'Bergen event' falls outside the 95% confidence region. It should be noted, however, that the Bergen event occurred at a hypocentral distance of roughly 1 km.

To investigate whether or not the Bergen event is consistent with the magnitude frequency distribution of catalogued events, the viewing bias (section 6.1) has to be accounted for. The viewing bias at 1 km distance yields a threshold magnitude of M_w=-2.2, implying that events with M_w<-2.2 have to be excluded from the statistical analysis. Figure 17 shows the magnitude-frequency distribution for the remaining events. The b-value reduced to b=0.85 and the Bergen event lies just inside the 95% confidence range. The quality of the data fit is

relatively poor, which may be explained by the small size of the data catalogue. In particular we note that M_c (red dot in Figure 17) lies underneath the fitting line indicating poor match of the lower magnitudes.

Considering that the confidence range might be underestimated due to an additional error-contribution associated with instrument downtimes (compare section 6.1) and recognizing that the magnitude of the Bergen event itself is associated with some uncertainty, we conclude that the magnitude of the Bergen event is not unexpectedly high on the 2σ confidence level.

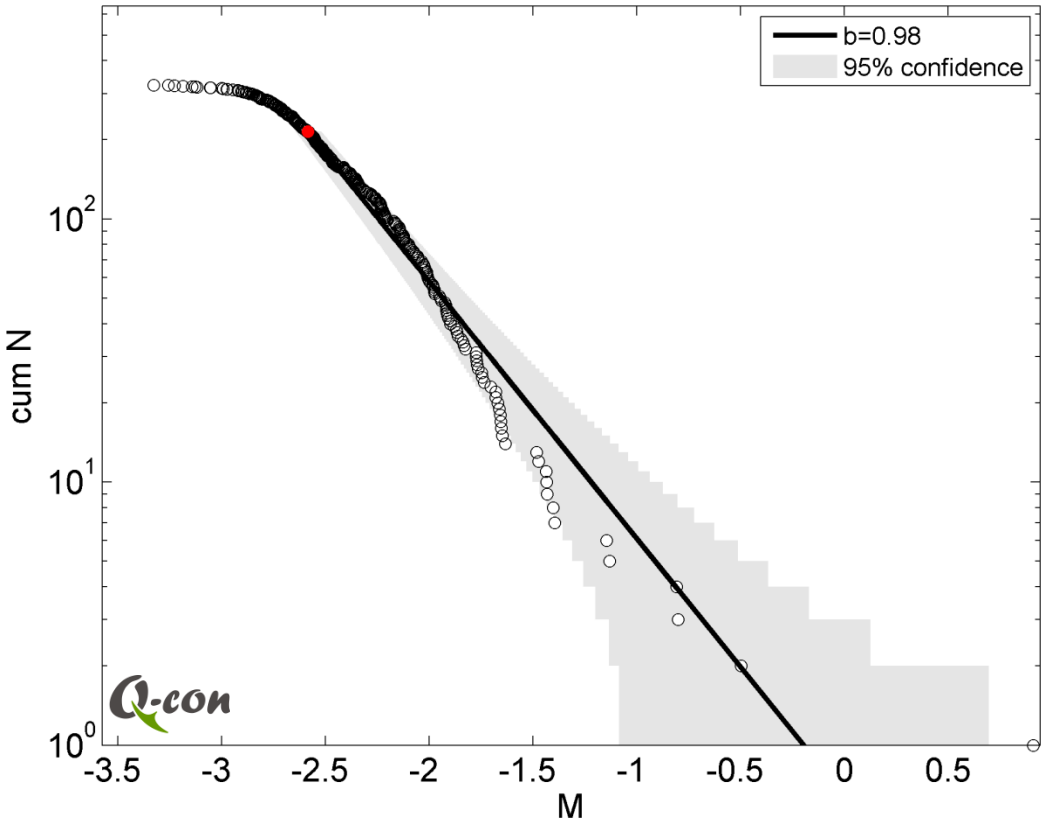

Figure 16: Magnitude frequency distribution of those 323 reservoir events for which hypocenter locations could be determined. Line fit indicates b=0.98, red dot denotes magnitude of completeness M_c determined from maximum curvature (e.g. Wiemer & Wyss, 2000). No viewing bias has been considered.

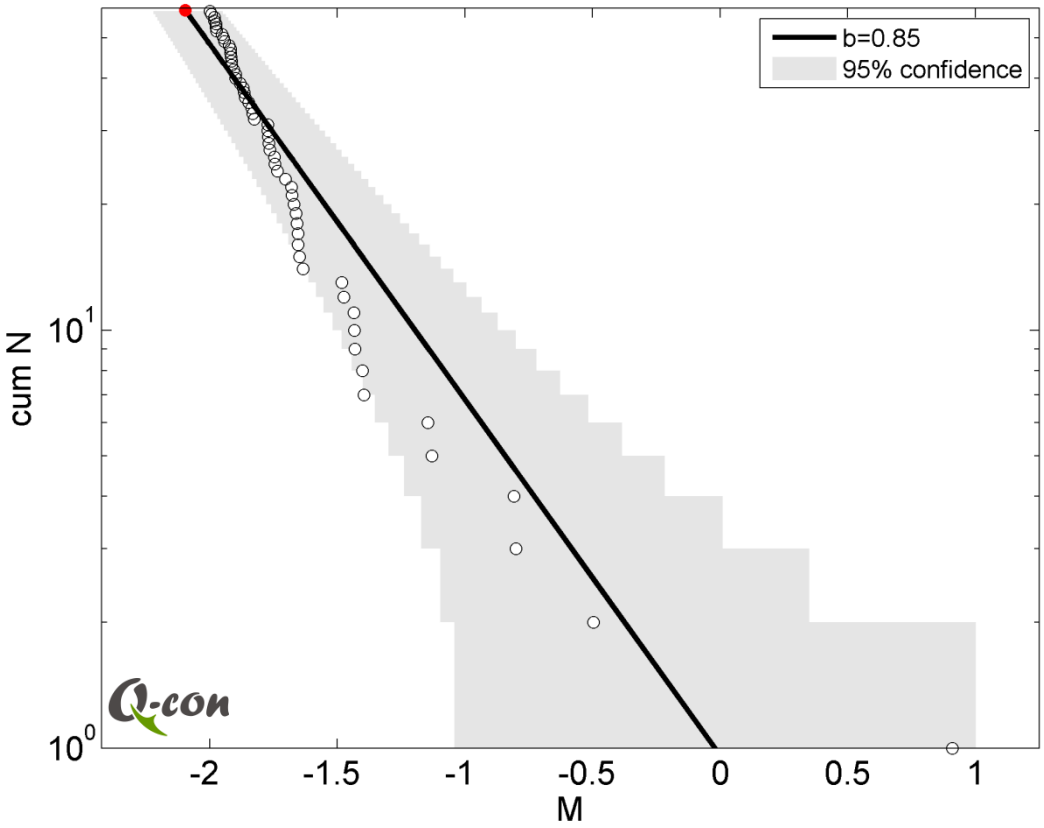

Figure 17: Same as previous figure while limiting the data set to events with $M_w \geq -2.2$.

6.3 Implications for Traffic Light System

For operating the gas storage facility at Bergermeer, a 'traffic light system (TLS)' is in place with the stop-light defined at M_L=3.5. Similar TLS are used for limiting the strength of induced seismicity in different energy technologies. They provide today's most effective mitigation measure for seismic risk, although a failure-free performance is not guaranteed. In particular, large 'jumps' in the temporal evolution of earthquake strength, as well as post-operational seismicity[2] may cause TLS failure.

The temporal evolution of maximum event magnitudes during refill of the Bergermeer reservoir (Figure 11) exhibits two larger jumps of $\Delta M_w \approx 1.5$. These, however, occurred at a low magnitude level, i.e. from M_w=-2 to M_w=-0.5 and M_w=-0.5 to M_w=0.9. In terms of radiated seismic energy, the latter jump corresponds to an energy increase from approximately 5 kJ to 500 kJ.

At a higher magnitude level, a similar jump of 1.5 magnitude units is associated with a much

[2] Considering post-operational seismicity requires geomechanical modelling, which is not part of the current study.

larger energy increase. For example, a jump from M_L=2 (in between TLS yellow and TLS orange) to M_L=3.5 (TLS red) corresponds to a seismic energy increase of approximately 50,000,000 kJ. The relatively large magnitude jumps observed at the low magnitude level are not indicating that similar magnitude jumps need to be expected at higher levels, where the TLS may still be robust.

7 SEISMICITY INTERPRETATION

The observed seismicity plays a crucial role for understanding the mechanical behavior of the Bergermeer reservoir and for assessing the seismic hazard associated with future reservoir operations. In absence of *in situ* stress measurements, observed seismicity during refill provides important constraints on stress paths in the reservoir. Although the development of a full geomechanical model is beyond the scope of the current analysis, we outline in the following, how seismicity observations can be used for calibrating a geomechanical model of the Bergermeer reservoir.

Our strategy rests on a basic concept of the physical processes leading to induced seismicity. It is not tied to a specific set of model parameters (e.g. spatial distribution of reservoir transmissibility), which may change in the course of currently ongoing geomechanical interpretations.

7.1 Conceptual Model

The starting point for our conceptual model is the assumption that seismicity is solely controlled by induced stresses due to reservoir compaction or re-filling. Tectonic stresses acting on faults in the Bergermeer region are assumed to be significantly below stress criticality. This assumption is motivated by the absence of natural earthquakes in the Bergermeer region (Dost & Haak, 2007).

The Bergermeer reservoir showed pronounced seismic activity during depletion with four earthquakes of magnitude M_L=3 to M_L=3.5 (Kraaijpoel et al., 2011). Only few local monitoring stations were operated at the time when these earthquakes occurred, leaving some uncertainty regarding hypocenter locations. It is, however, likely that these earthquakes occurred near the region of maximum differential compaction on the main fault (Kraaijpoel et al., 2011), i. e. fault number 13 in Figure 7.

The condition for failure and the onset of fault slip can be expressed by

Equation 1: $\tau_{crit}=\mu\,(\sigma_n-p)+\tau_0$

with τ_{crit} denoting critical shear stress on the fault, σ_n normal stress, p *in situ* pressure, μ the coefficient of friction, and τ_0 cohesion.

Although reservoir stresses during production are largely unknown, we nevertheless can assume that those fault patches which were seismically activated during production remain critically stressed: After an induced earthquake has occurred, the stress state on the associated slip area is controlled by the amount of stress consumed during the earthquake process, i.e. primarily by lowering of the shear stress. The coseismic stress drop of induced earthquakes is typically small compared to the total stress acting on a fault (e.g. Jost et al., 1998; Baisch & Harjes, 2003). Therefore stress conditions on a rupture plane remain close to criticality, within 0.1 MPa up to a few Megapascals, after an induced earthquake has occurred. This is the most important aspect of our conceptual model.

In general, two driving processes for inducing seismicity in the Bergermeer reservoir are considered (e.g. TNO, 2014). Firstly, (differential) compaction during production may cause overcritical conditions. This happens despite the locking effect associated with lowering reservoir pressure, since shear- and normal-stress are also depending on reservoir pressure (poro-elasticity). And secondly, reservoir pressure increase during refill can also induce seismicity according to Equation 1. The latter mechanism requires some sort of time-dependency (see Figure 18). For example, if the *in situ* pressure on a seismogenic fault increases faster during refill than the poro-elastic counterbalancing effects in the rock matrix (i.e. the combination of decreasing shear stress and increasing normal stress) due to channeling, then the fault may fail again during refill. Alternatively, hysteresis may cause anelasticity and associated time-dependency. The latter effect has been used to successfully model the observed delay of surface uplift during refill (pers. comm. dePater, January 2016).

In our conceptual model, however, we do not have to discriminate between the possible mechanisms for time-dependency. The most important aspects of our conceptual model are

- seismicity during refill occurs on the main faults at those locations, which were already seismically active during production (this is consistent with observations, e.g. Figure 7),
- the failure mechanism of the seismicity induced during refill is the same as during production (i.e. seismic slip vectors are parallel).

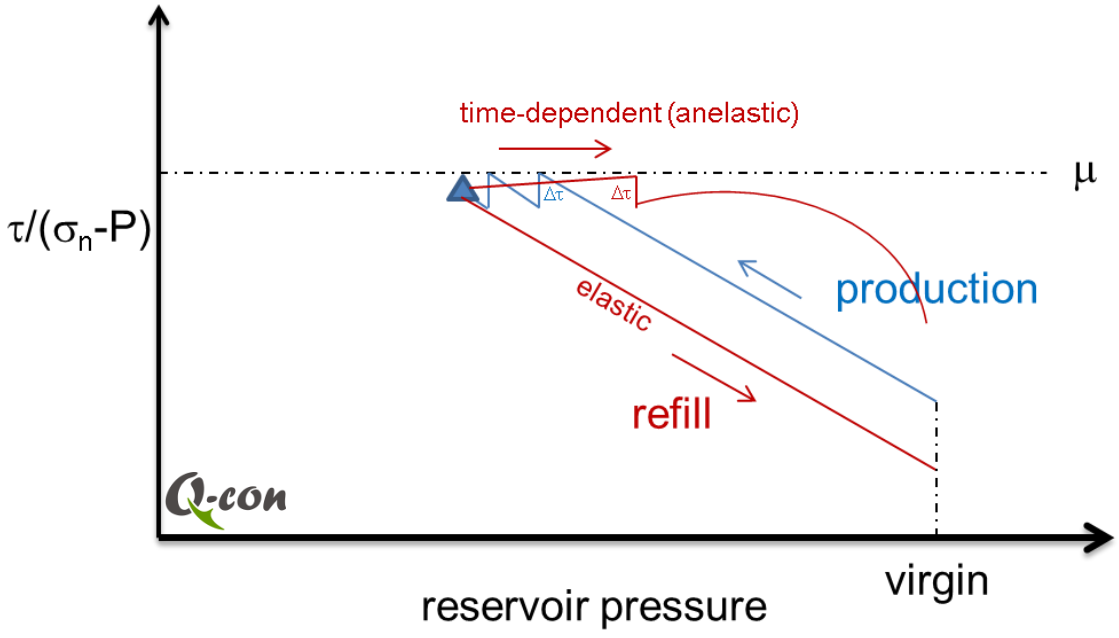

Figure 18: Sketch illustrating stress conditions on a reservoir fault during production (blue) and re-fill (red). During production, the stress path reaches criticality (μ) due to differential compaction. Shear stress is lowered (repeatedly) by $\Delta\tau$ due to seismic or aseismic deformations. During refill, the fault can be stabilized (elastic model) or reach stress criticality again, if pressure on the fault increases faster than the counterbalancing effects.

7.2 Indicators for Localized Stress Concentrations

The magnitude of an induced event is controlled by the fault area over which overcritical stress conditions are reached at the time when the event occurs, including the co-seismic (dynamic) stress redistribution. From a seismic hazard perspective, the most important scenario is associated with a systematic increase of the shear to effective normal stress ratio (Equation 1) over a larger fault area.

The spatio-temporal seismicity distribution observed (to date) during refill, however, shows no indications of such a larger scale increase of stress-criticality. On the contrary, seismic activity appears strongly clustered in space and time, with regions of previous seismic activity becoming 'silent' at a later stage during refill.

This is most evident in Figure 19 showing the timeline of clustered events. Cluster timelines are representative for the seismic activity in a particular reservoir region. Most timelines are of extremely short duration (mostly within the range of hours), indicating that overcritical stress conditions at the associated reservoir locations were reached only in a short period of time.

Furthermore, the slip area of the reservoir events observed during refill ranges from <1 m^2 to approx. 1,500 m^2 (Bergen event). This is only a tiny (<1%) fraction of the slip area associated with production induced seismicity (an M_L=3.5 earthquake typically has a slip area of approx. 600,000 m^2), demonstrating that spatial regions exceeding stress criticality were localized at or below the decameter level during refill (until to date).

We found another indication for localized stress concentrations in terms of stress heterogeneities. Figure 20 shows the waveform section of a 'double event' sequence. Within 20 milliseconds, two events occurred at approximately the same location. Their P-wave polarity, however, is opposite indicating a different failure mechanism. It is likely that the first event triggered the second one, because two further, almost identical double event sequences followed within 5 minutes. We interpret these double event sequences as an expression of spatially localized stress heterogeneities at the intersection between faults 1 and 13.

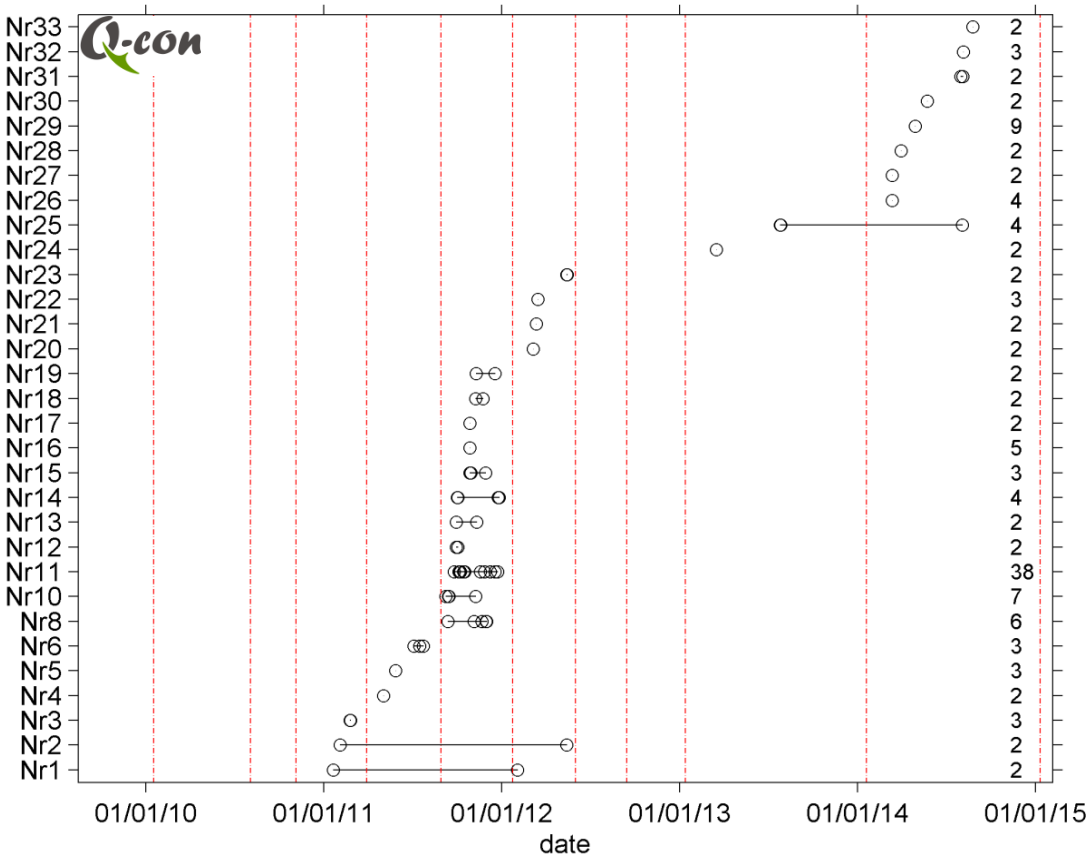

Figure 19: Time line of events belonging to the 31 clusters deduced from Figure 5. The (non-continuous) cluster ID is indicated on the y-axis. Occurrence times of events are denoted by open circles. Events belonging to the same cluster are connected by a solid (horizontal) line. Many clusters appear as a single circle due to their extremely short duration. The number of events belonging to each individual cluster is annotated on the right hand side. Dashed vertical lines indicate different monitoring periods.

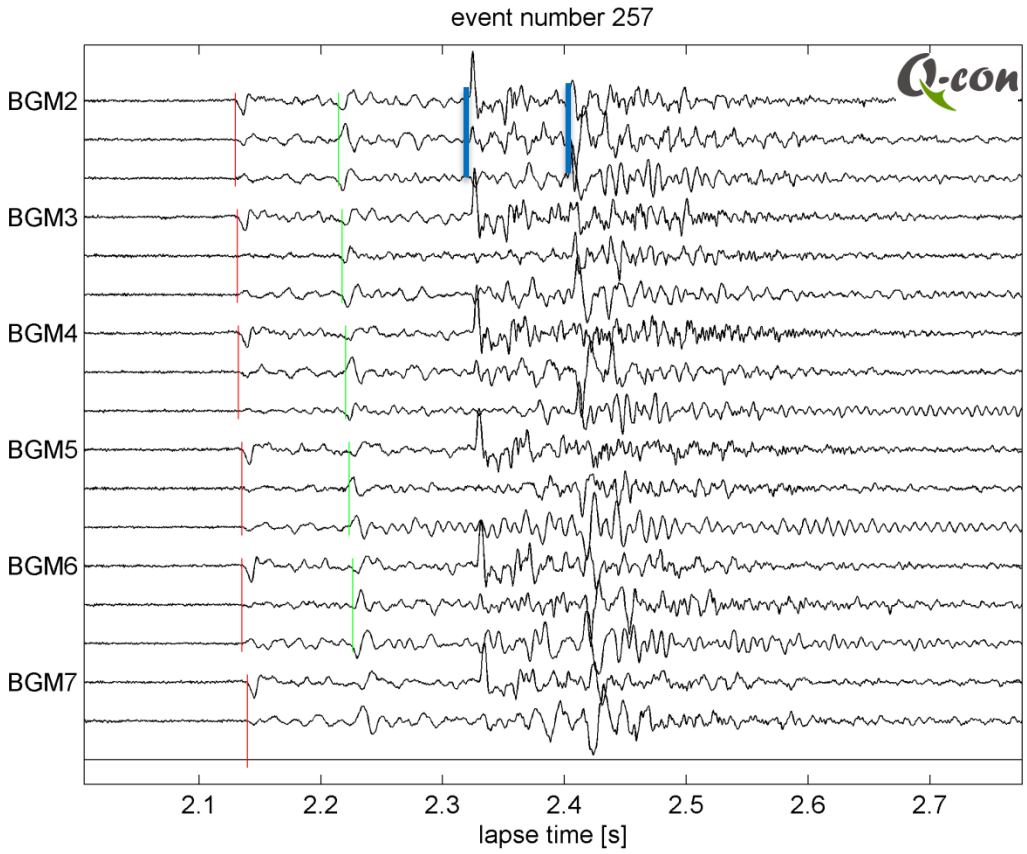

Figure 20: Seismogram recordings of event number 257 recorded by the six 3-component downhole geophones. P- and S-phase onsets are marked in red and green, respectively. A second event (258) has occurred approx. 0.2 s later (P- and S-phase onsets at BGM2 are indicated in blue). Both events are almost co-located. The P-wave polarity of the two events, however, is opposite.

7.3 Geometrical Interpretation

We use the fault collapsed hypocenter distribution (chapter 5), which represents our preferred structural interpretation, to further investigate the spatio-temporal evolution of seismicity and compare it to reservoir pressure. Figure 21 shows the temporal evolution of event magnitudes, where color encoding denotes associated faults.

Temporal event clusters can be clearly identified: Seismicity on fault number 11 started at the beginning of the monitoring period, but vanished after the end of 2012. Seismicity on fault number 10 is constrained to the time period from the end of 2013 to the end of 2014. Despite two scattered events, activity on fault number 1 is constrained to the year 2014.

The main fault (number 13) and the eastern fault (number 12) do not show this clear type of temporal clustering in the overview plot (Figure 21). These faults, however, extend over several kilometers. A more detailed analysis of the seismicity on these faults shows the same distinct temporal clustering (Figure 22, Figure 23). On both faults we notice a clear North-

South migration of seismic activity with time. Despite some data scattering, it seems that several clusters of seismic activity become seismically silent after a certain point in time, despite the almost continuously increasing reservoir pressure.

On the smaller faults (1, 10, 11), seismicity clusters both in space and in time (Figure 24, Figure 25).

Figure 26 shows the temporal evolution of all events exhibiting a similar North-South trend. To account for the viewing bias, events with $M_w \leq -2.2$ (corresponding to the viewing limit at 1 km hypocentral distance) are assigned a smaller symbol size. The North-South trend remains even when considering only events with $M_w > -2.2$. This confirms that the temporal migration of seismicity is not an artifact from changing the monitoring well.

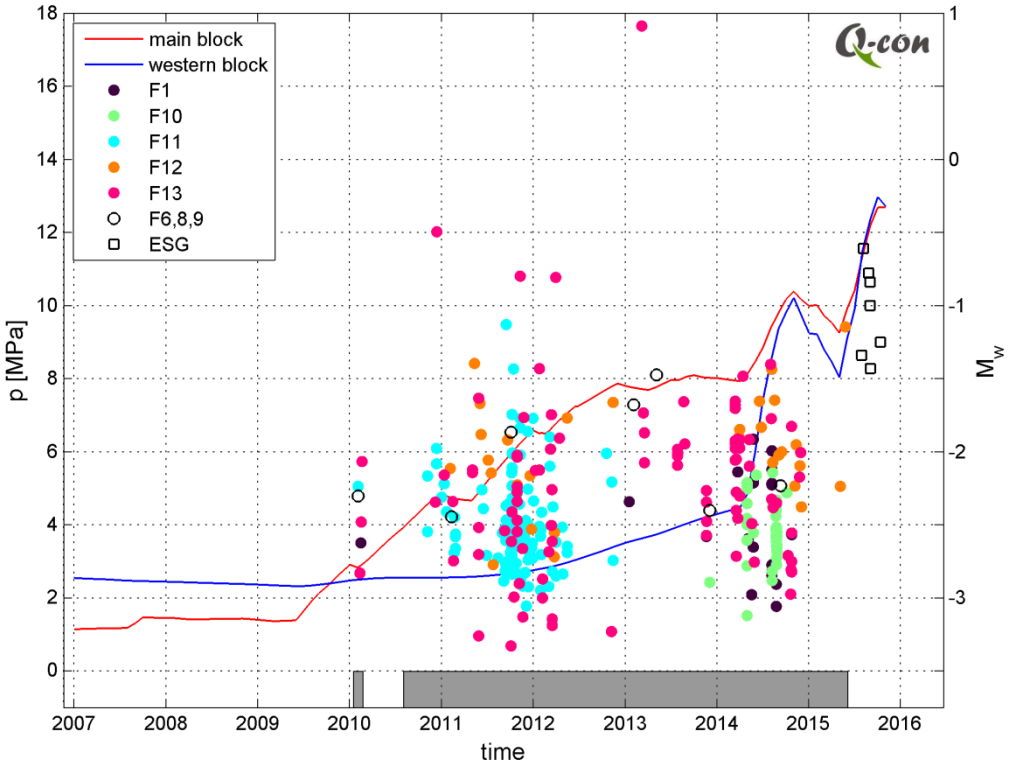

Figure 21: Temporal evolution of seismic event magnitudes (dots). Red and blue lines denote average reservoir pressure in the main and western block. Shaded bar at the bottom indicates time intervals during which seismic monitoring was performed. Smaller downtimes up to several days are not shown (these can be found in Appendix A of TAQA002). Seven events monitored by ESG are shown by open squares. These occurred after the monitoring period considered here and were thus not quality controlled.

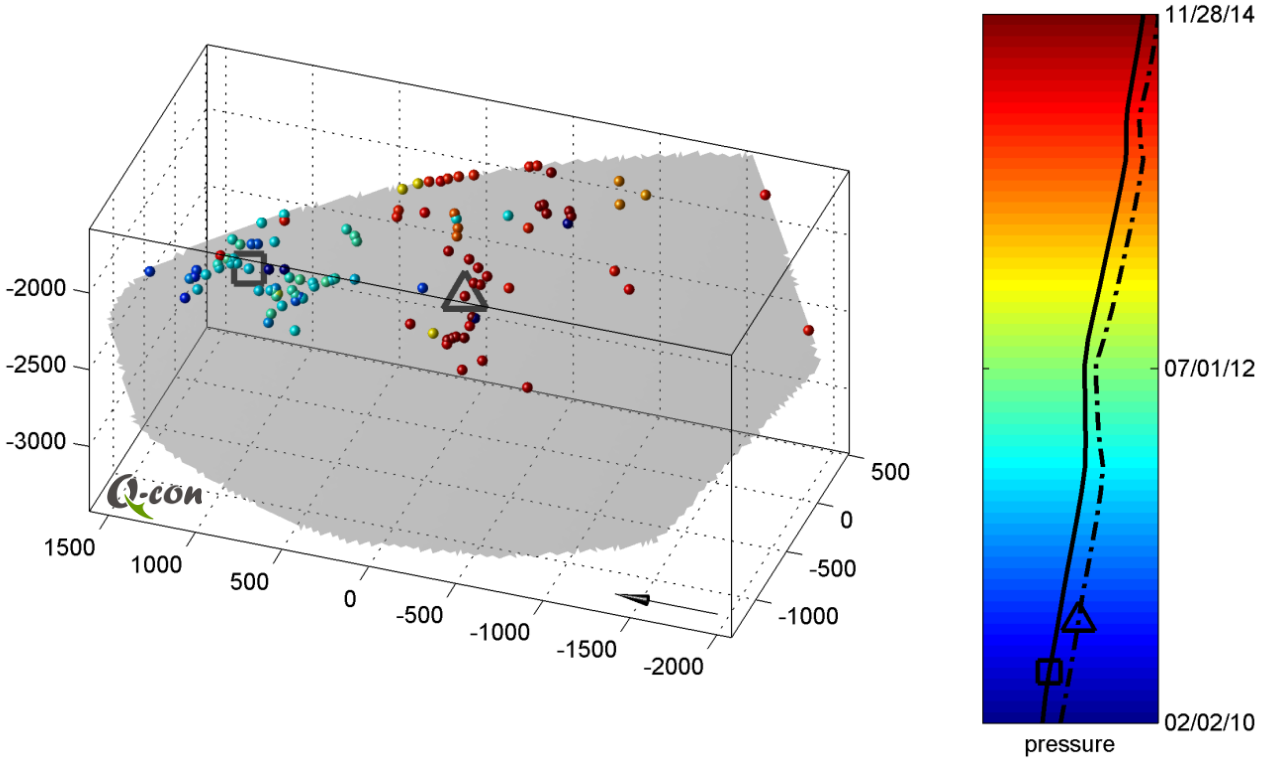

Figure 22: Spatio-temporal evolution of fault-collapsed seismicity on the main fault (number 13). Color encoding denotes event occurrence time. Relative pressure evolution at two reference points (indicated by a square and a triangle, respectively) is shown by a solid and dash-dotted line embedded in the colorbar.

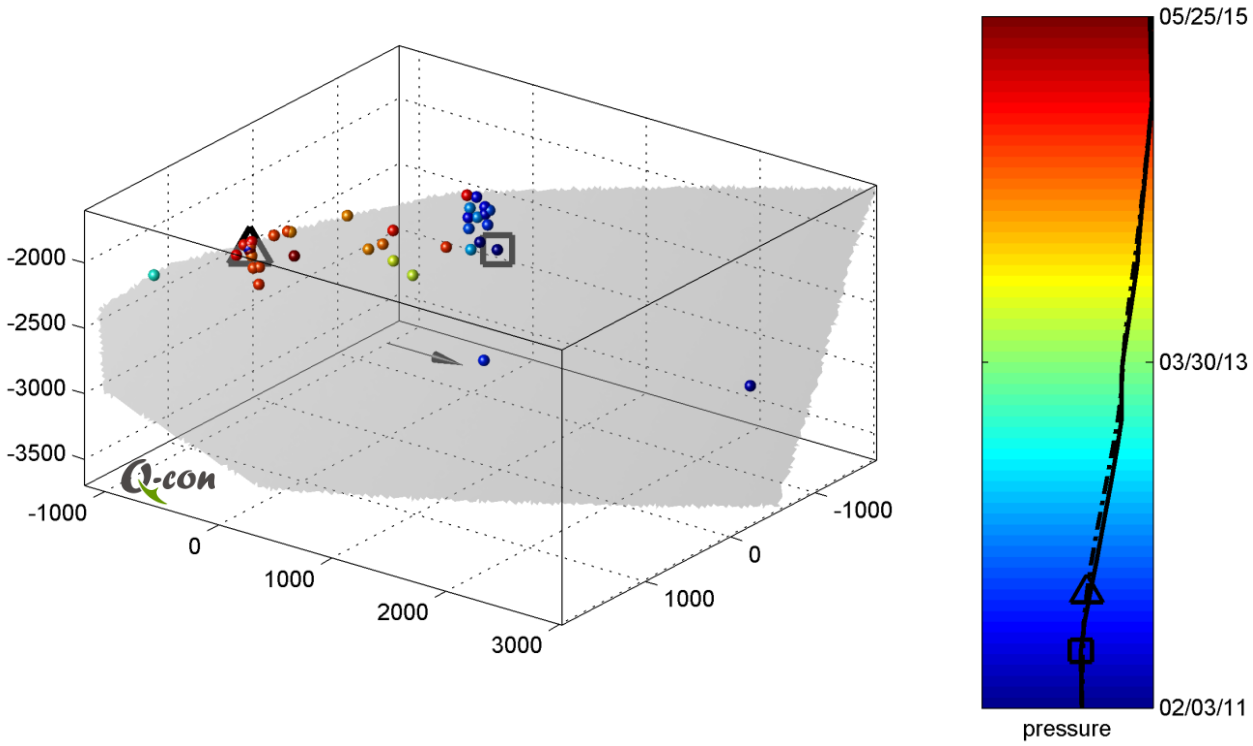

Figure 23: Spatio-temporal evolution of fault-collapsed seismicity on fault number 12. Color encoding denotes event occurrence time. Relative pressure evolution at two reference points (indicated by a square and a triangle, respectively) is shown by a solid and dash-dotted line embedded in the colorbar.

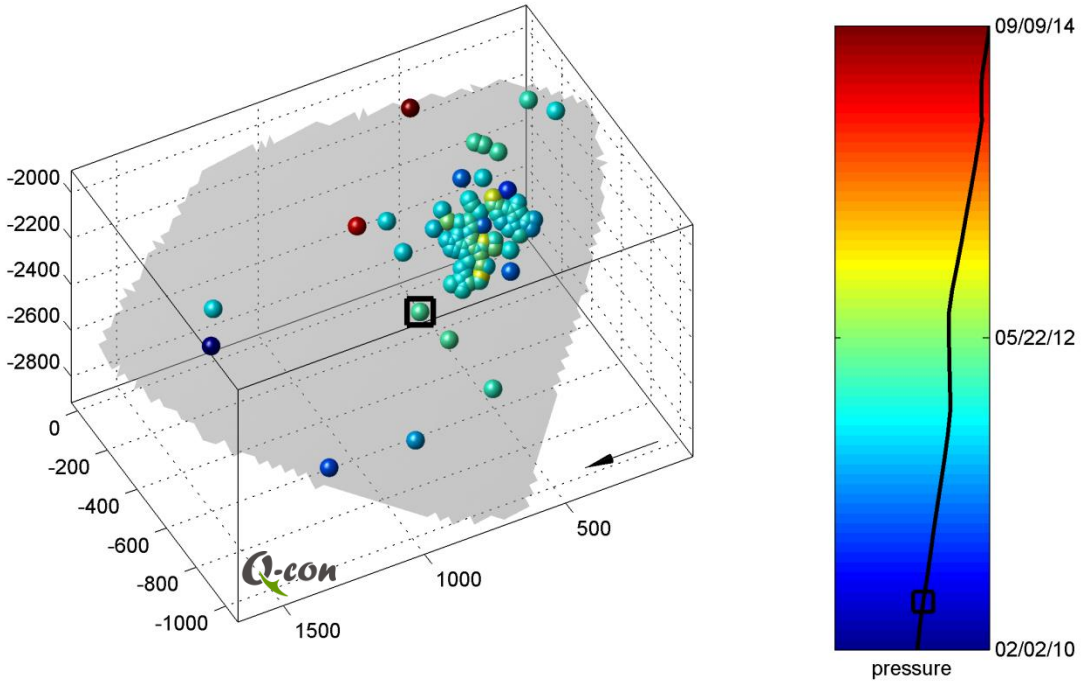

Figure 24: Spatio-temporal evolution of fault-collapsed seismicity on fault number 11. Color encoding denotes event occurrence time. Relative pressure evolution at a reference point (indicated by a square) is shown by a solid line embedded in the colorbar.

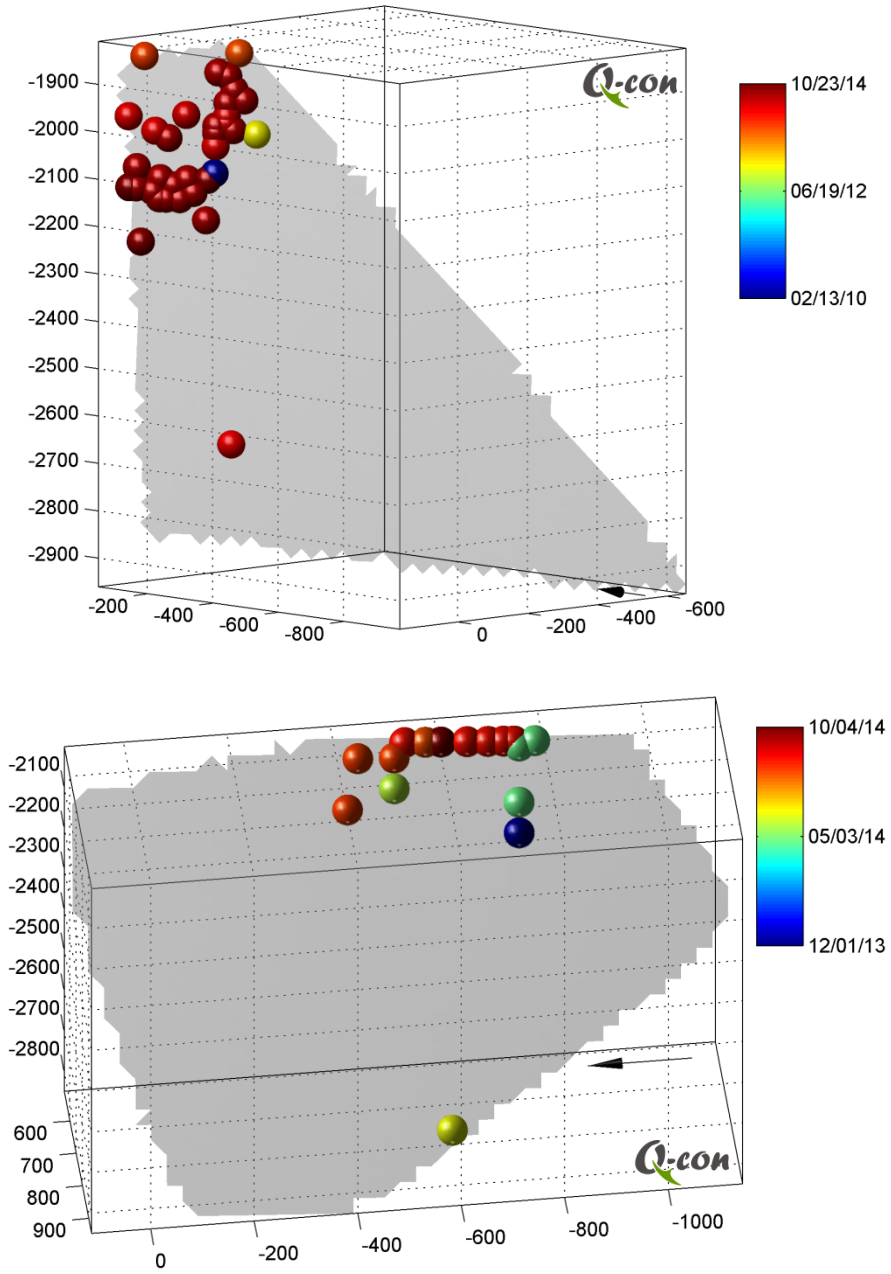

Figure 25: Spatio-temporal evolution of fault-collapsed seismicity on fault number 1 (top) and fault number 10 (bottom). Color encoding denotes event occurrence time according to the color maps.

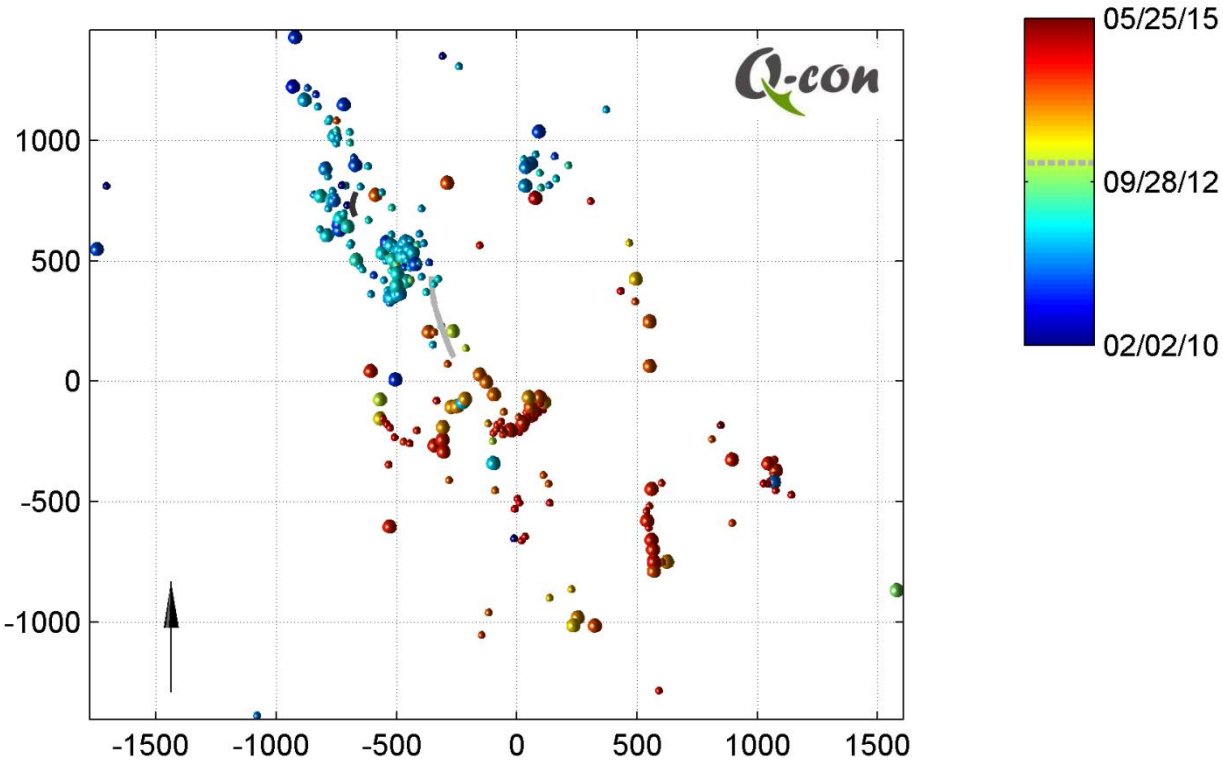

Figure 26: Nearest-fault collapsed hypocenter distribution in map view. Color encoding denotes occurrence time according to the colormap. Events with M_w ≤-2.2 are displayed by a smaller sphere than those with M_w >-2.2.Wellbore trajectories of BGM03a and BGM05 are shown by a black and grey line, respectively. Additionally, the time of changing the monitoring wells is indicated by a dashed line embedded into the colorbar.

REFERENCES

Baisch, S., Bohnhoff, M., Ceranna, L., Tu, Y., and H.-P.Harjes, 2002. Probing the crust to 9 km depth: Fluid injection experiments and induced seismicity at the KTB superdeep drilling hole, Germany. *Bull. Seism. Soc. Amer.*, **92**, 2369 – 2380.

Baisch, S., and H.-P.Harjes, 2003. A model for fluid injection induced seismicity at the KTB. *Geophys. Jour. Int.*, **152**, 160-170.

Baisch, S., Ceranna, L., and H.-P.Harjes, 2008. Earthquake Cluster: What can we learn from waveform similarity? *Bull. Seism. Soc. Amer.*, **98**, 2806 – 2814.

Bulut, F., Bohnhoff, M., Ellsworth, W. L., Aktar, M., and G. Dresen, 2009. Microseismicity at the North Anatolian Fault in the Sea of Marmara offshore Istanbul, NW Turkey. *J. Geophys. Res.*, **114**, doi:10.1029/2008JB006244, 2009.

Dost, B. and H.W. Haak, 2007. Natural and induced seismicity, in Th. E. Wong, D.A.J. Batjes, and J. de Jager, eds., *Geology of the Netherlands*, Royal Netherlands Academy of Arts and Sciences, 223-229

Dost, B., Goutbeck, F., van Eck, T., and D. Kraaijpoel, 2012. Monitoring induced seismicity in the North of the Netherlands, status report 2010. *KNMI Scientific report*, WR 2012-03, DeBilt, 2012.

Eaton, D.W., Davidsen, J., Pedersen, P.K., and N. Boroumand, 2014. Breakdown of the Gutenberg-Richter relation for microearthquakes induced by hydraulic fracturing: influence of stratabound fractures. *Geophysical Prospecting,* **62**(4), 806-818.

Hanks, T. C. and H. Kanamori, 1979. A moment magnitude scale. *J. Geophys. Res.*, **84**, 2348-2350.

Jones, R. H., and R. C. Stewart, 1997. A method for determining significant structures in a cloud of earthquakes. J. Geophys. Res., **102**(B4), 8245-8254.

Jost, M.L., Büßelberg, T., Jost, Ö., and Harjes, H.-P., 1998. Source parameters of injection-induced microearthquakes at 9 km depth at the KTB deep drilling site, Germany. Bull. Seism. Soc. Amer., 88(3), 815-832.

Jurkevics, A., 1988. Polarization analysis of three-component array data. *Bull. Seism. Soc. Amer.*, **78**(5), 1725-1743.

Kraaijpoel, D., Kwee, J., and B. Dost, 2011. Microseismic monitoring of an underground gas storage facility in the Netherlands. *Geophysical Research Abstracts*, **13**, EGU2011-13477.

References

Poupinet, G., Ellsworth, W., and J. Frechet, 1984. Monitoring velocity variations in the crust using earthquake doublets: An application to the Calaveras Fault, California. *J. Geophys. Res.*, **89**, 5719-5731.

TAQA002. Induced Seismicity in the Bergermeer Field: WP1 - Quality Control. *Q-con report to Taqa Energy B.V.*, 30th November 2015, 34 pages.

TNO, 2014. Literature review on injection-related induced seismicity and its relevance to nitrogen injection. TNO report, TNO2 2014 R11761, 46 pages.

Wiemer, S., and M. Wyss, 2000. Minimum Magnitude of Completeness in Earthquake Catalogs: Examples from Alaska, the Western united States, and Japan. *Bull. Seism. Soc. Amer.*, **90**, 859-869.

APPENDIX A SENSOR ORIENTATIONS

A.1. Test Phase

level	U	level	U
1	-0.9216 0.3873 0.0258 -0.3723 -0.8633 -0.3406 -0.1097 -0.3235 0.9398	4	-0.9105 0.4128 0.0258 -0.3962 -0.8526 -0.3406 -0.1187 -0.3203 0.9398
2	-0.8672 0.4972 0.0258 -0.4752 -0.8113 -0.3406 -0.1485 -0.3077 0.9398	5	-0.6436 0.7649 0.0258 -0.7250 -0.5986 -0.3406 -0.2451 -0.2379 0.9398
3	-0.9748 0.2215 0.0258 -0.2169 -0.9148 -0.3406 -0.0519 -0.3376 0.9398	6	0.6735 -0.7388 0.0258 0.7007 0.6269 -0.3406 0.2355 0.2475 0.9398

Table 1: Operator U to rotate the 6 downhole geophones from instrument system E' N' Z' into the true E N Z coordinate frame.

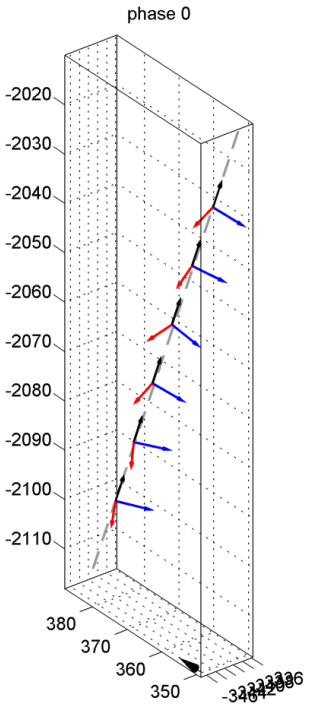

Figure 27: Tool orientations (black: vertical axis) and well trajectory (grey) in perspective view.

A.2. Phase 2

level	U	level	U
1	0.1213 -0.9920 -0.0354 0.9886 0.1239 -0.0854 0.0891 -0.0247 0.9957	4	-0.8740 -0.4847 -0.0354 0.4858 -0.8699 -0.0854 0.0106 -0.0919 0.9957
2	-0.7513 0.6591 -0.0354 -0.6548 -0.7510 -0.0854 -0.0829 -0.0410 0.9957	5	-0.6616 0.7490 -0.0354 -0.7447 -0.6619 -0.0854 -0.0874 -0.0301 0.9957
3	-0.2195 0.9750 -0.0354 -0.9713 -0.2218 -0.0854 -0.0911 0.0157 0.9957	6	0.7637 -0.6446 -0.0354 0.6403 0.7633 -0.0854 0.0821 0.0426 0.9957

Table 2: Operator U to rotate the 6 downhole geophones from instrument system E' N' Z' into the true E N Z coordinate frame.

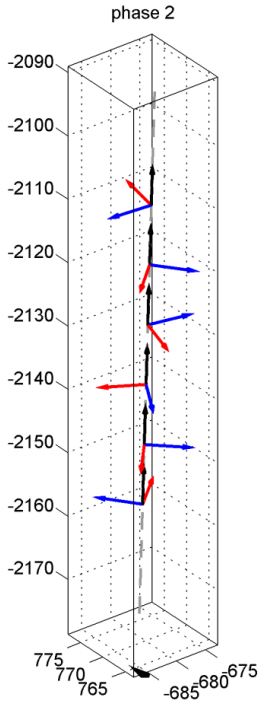

Figure 28: Tool orientations (black: vertical axis) and well trajectory (grey) in perspective view.

A.3. Phase 3

level	U	level	U
1	low SNR	4	-0.7951 -0.6055 -0.0354 0.6060 -0.7908 -0.0854 0.0237 -0.0894 0.9957
2	-0.4998 -0.8654 -0.0354 0.8643 -0.4957 -0.0854 0.0564 -0.0733 0.9957	5	-0.8636 -0.5029 -0.0354 0.5040 -0.8595 -0.0854 0.0125 -0.0916 0.9957
3	-0.9132 0.4060 -0.0354 -0.4020 -0.9116 -0.0854 -0.0670 -0.0638 0.9957	6	-0.9640 -0.2636 -0.0354 0.2657 -0.9603 -0.0854 -0.0115 -0.0918 0.9957

Table 3: Operator U to rotate the 6 downhole geophones from instrument system E' N' Z' into the true E N Z coordinate frame.

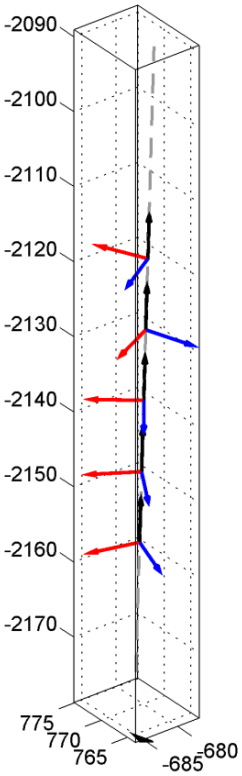

Figure 29: Tool orientations (black: vertical axis) and well trajectory (grey) in perspective view.

A.4. Phase 4

level	U	level	U
1	-0.9511 -0.3067 -0.0354 0.3087 -0.9473 -0.0854 -0.0074 -0.0922 0.9957	4	-0.5030 -0.8635 -0.0354 0.8624 -0.4989 -0.0854 0.0561 -0.0735 0.9957
2	0.3223 -0.9460 -0.0354 0.9421 0.3242 -0.0854 0.0923 -0.0058 0.9957	5	-0.9495 0.3119 -0.0354 -0.3080 -0.9475 -0.0854 -0.0602 -0.0702 0.9957
3	-0.8013 0.5972 -0.0354 -0.5930 -0.8007 -0.0854 -0.0794 -0.0474 0.9957	6	-0.9799 0.1964 -0.0354 -0.1929 -0.9775 -0.0854 -0.0514 -0.0769 0.9957

Table 4: Operator U to rotate the 6 downhole geophones from instrument system E' N' Z' into the true E N Z coordinate frame.

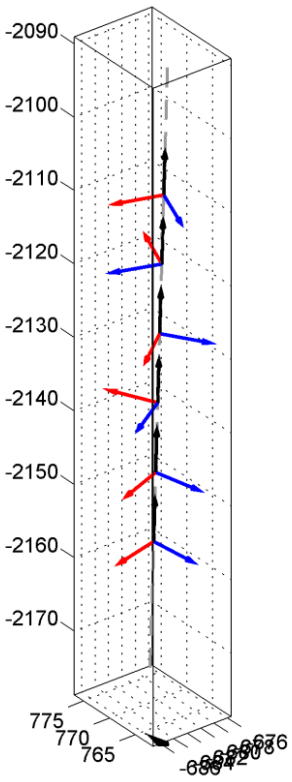

Figure 30: Tool orientations (black: vertical axis) and well trajectory (grey) in perspective view.

A.5. Phase 5

level	U	level	U
1	0.1069 -0.9936 -0.0354 0.9903 0.1096 -0.0854 0.0888 -0.0260 0.9957	4	-0.2415 0.9698 -0.0354 -0.9661 -0.2437 -0.0854 -0.0915 0.0136 0.9957
2	-0.9285 0.3695 -0.0354 -0.3656 -0.9269 -0.0854 -0.0644 -0.0664 0.9957	5	-0.8936 -0.4474 -0.0354 0.4488 -0.8896 -0.0854 0.0067 -0.0922 0.9957
3	-0.0891 0.9954 -0.0354 -0.9921 -0.0919 -0.0854 -0.0883 0.0275 0.9957	6	-0.8971 0.4404 -0.0354 -0.4364 -0.8957 -0.0854 -0.0694 -0.0612 0.9957

Table 5: Operator U to rotate the 6 downhole geophones from instrument system E' N' Z' into the true E N Z coordinate frame.

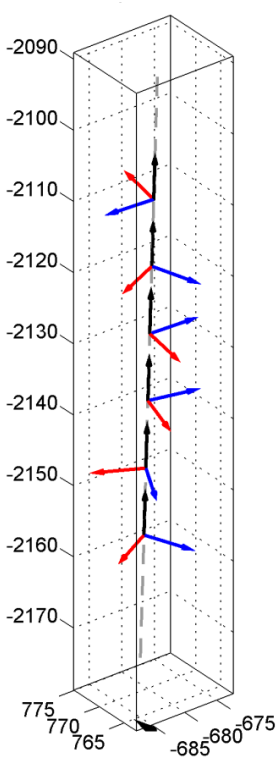

Figure 31: Tool orientations (black: vertical axis) and well trajectory (grey) in perspective view.

A.6. Phase 6

level	U	level	U
1	-0.4289 -0.9026 -0.0354 0.9012 -0.4249 -0.0854 0.0621 -0.0686 0.9957	4	-0.9931 0.1121 -0.0354 -0.1087 -0.9904 -0.0854 -0.0447 -0.0810 0.9957
2	-0.6397 0.7678 -0.0354 -0.7635 -0.6401 -0.0854 -0.0883 -0.0276 0.9957	5	-0.6854 -0.7273 -0.0354 0.7272 -0.6811 -0.0854 0.0380 -0.0843 0.9957
3	-0.7307 -0.6818 -0.0354 0.6820 -0.7264 -0.0854 0.0325 -0.0866 0.9957	6	0.6581 -0.7521 -0.0354 0.7479 0.6583 -0.0854 0.0876 0.0297 0.9957

Table 6: Operator U to rotate the 6 downhole geophones from instrument system E' N' Z' into the true E N Z coordinate frame.

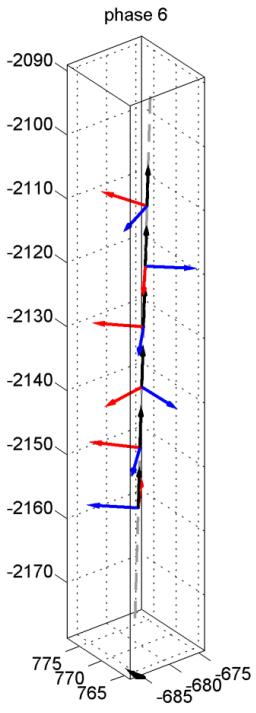

Figure 32: Tool orientations (black: vertical axis) and well trajectory (grey) in perspective view.

A.7. Phase 7

level	U	level	U
1	-0.1567 -0.9870 -0.0354 0.9845 -0.1533 -0.0854 0.0789 -0.0483 0.9957	4	-0.9993 -0.0149 -0.0354 0.0179 -0.9962 -0.0854 -0.0340 -0.0860 0.9957
2	-0.3807 -0.9240 -0.0354 0.9224 -0.3768 -0.0854 0.0656 -0.0652 0.9957	5	-0.9771 -0.2096 -0.0354 0.2119 -0.9735 -0.0854 -0.0166 -0.0910 0.9957
3	-0.8551 -0.5172 -0.0354 0.5182 -0.8510 -0.0854 0.0140 -0.0914 0.9957	6	-0.9386 -0.3432 -0.0354 0.3450 -0.9347 -0.0854 -0.0038 -0.0924 0.9957

Table 7: Operator U to rotate the 6 downhole geophones from instrument system E' N' Z' into the true E N Z coordinate frame.

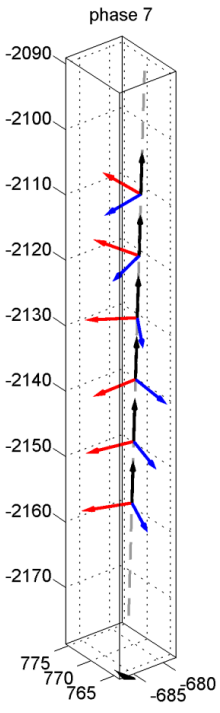

Figure 33: Tool orientations (black: vertical axis) and well trajectory (grey) in perspective view.

A.8. Phase 8

level	U	level	U
1	0.7550 -0.6113 -0.2371 0.6467 0.6349 0.4226 -0.1078 -0.4725 0.8747	4	0.7303 0.6407 -0.2371 -0.5163 0.7449 0.4226 0.4474 -0.1862 0.8747
2	0.9305 0.2792 -0.2371 -0.1600 0.8921 0.4226 0.3295 -0.3553 0.8747	5	-0.3738 -0.8967 -0.2371 0.7914 -0.4416 0.4226 -0.4837 -0.0297 0.8747
3	-0.0817 -0.9680 -0.2371 0.8885 -0.1785 0.4226 -0.4515 -0.1762 0.8747	6	0.3357 -0.9116 -0.2371 0.8806 0.2144 0.4226 -0.3345 -0.3507 0.8747

Table 8: Operator U to rotate the 6 downhole geophones from instrument system E' N' Z' into the true E N Z coordinate frame.

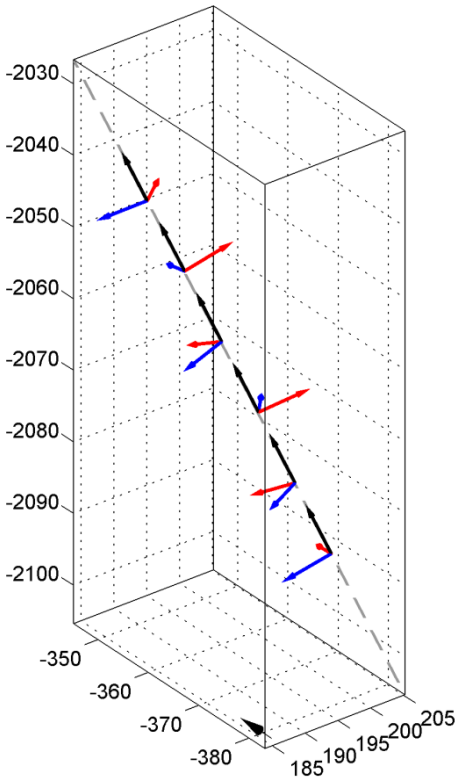

Figure 34: Tool orientations (black: vertical axis) and well trajectory (grey) in perspective view.

A.9. Phase 9

level	U	level	U
1	0.8050 -0.5439 -0.2371 0.5896 0.6883 0.4226 -0.0667 -0.4800 0.8747	4	-0.3626 -0.9013 -0.2371 0.7968 -0.4318 0.4226 -0.4833 -0.0357 0.8747
2	0.6697 0.7038 -0.2371 -0.5812 0.6954 0.4226 0.4623 -0.1453 0.8747	5	0.9377 0.2540 -0.2371 -0.1359 0.8961 0.4226 0.3198 -0.3641 0.8747
3	0.6834 -0.6905 -0.2371 0.7125 0.5601 0.4226 -0.1591 -0.4578 0.8747	6	0.3806 -0.8938 -0.2371 0.8688 0.2579 0.4226 -0.3166 -0.3669 0.8747

Table 9: Operator U to rotate the 6 downhole geophones from instrument system E' N' Z' into the true E N Z coordinate frame.

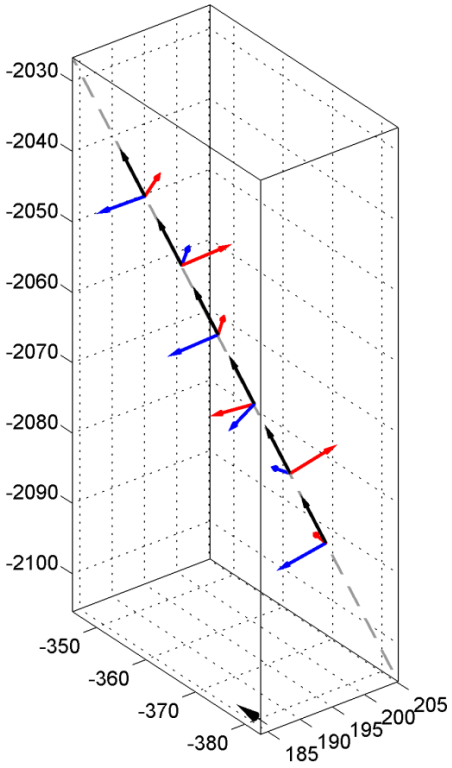

Figure 35: Tool orientations (black: vertical axis) and well trajectory (grey) in perspective view.

A.10. Phase 10

level	U	level	U
1	0.4895 -0.8391 -0.2371 0.8297 0.3646 0.4226 -0.2682 -0.4036 0.8747	4	-0.0924 -0.9671 -0.2371 0.8865 -0.1883 0.4226 -0.4534 -0.1711 0.8747
2	0.3960 -0.8871 -0.2371 0.8643 0.2728 0.4226 -0.3103 -0.3723 0.8747	5	0.6325 -0.7374 -0.2371 0.7506 0.5079 0.4226 -0.1912 -0.4453 0.8747
3	0.4626 -0.8543 -0.2371 0.8409 0.3381 0.4226 -0.2809 -0.3949 0.8747	6	-0.8358 0.4953 -0.2371 -0.5478 -0.7220 0.4226 0.0381 0.4831 0.8747

Table 10: Operator U to rotate the 6 downhole geophones from instrument system E' N' Z' into the true E N Z coordinate frame.

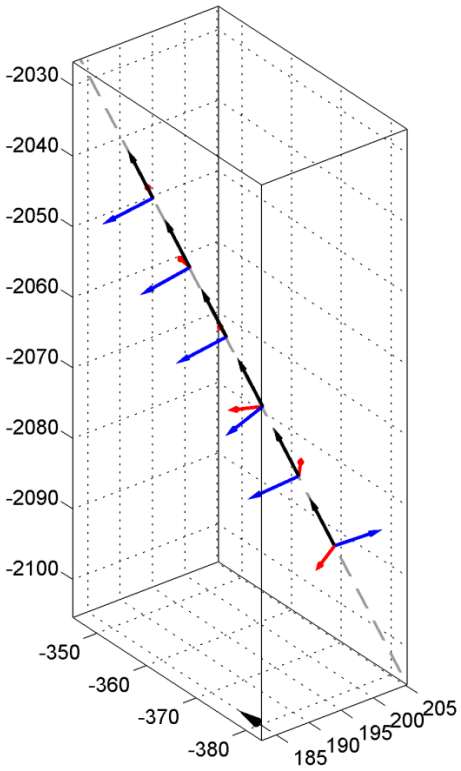

Figure 36: Tool orientations (black: vertical axis) and well trajectory (grey) in perspective view.

APPENDIX B MINIMUM COMPLEXITY MODEL

The fault collapsed hypocenter distribution (chapter 5) indicates that a certain subset of faults is seismically active during refill. These include faults number 1, 10, 11, 12, and 13 (main fault) where most activity occurs. In the following we refer to these faults as 'active faults'. Isolated events also occurred on faults 6, 8, and 9, but these may well reflect the large location errors associated with individual events.

To investigate if the subset of active faults could simply be an artifact resulting from a specific spatial distribution of mislocated events, we tested if the seismicity can be collapsed onto a smaller number of faults.

Starting with the main fault, we selected those 297 events, which can be moved onto the main fault (number 13) within their confidence limits. In a second step, we applied the same procedure to the remaining events and selected those events which can be 'collapsed' onto fault number 11. The same was repeated for fault number 12 and number 1, after which all events were collapsed onto faults (see statistic in Figure 37). Figure 38 shows the resulting hypocenter distribution.

This exercise demonstrates that only a single fault (number 10) from the set of active faults is not strictly required for fault collapsing. We note, however, that the seismicity on fault 10 (after nearest-fault collapsing) is strongly clustered in space and time (compare Figure 25) indicating that this fault was truly active.

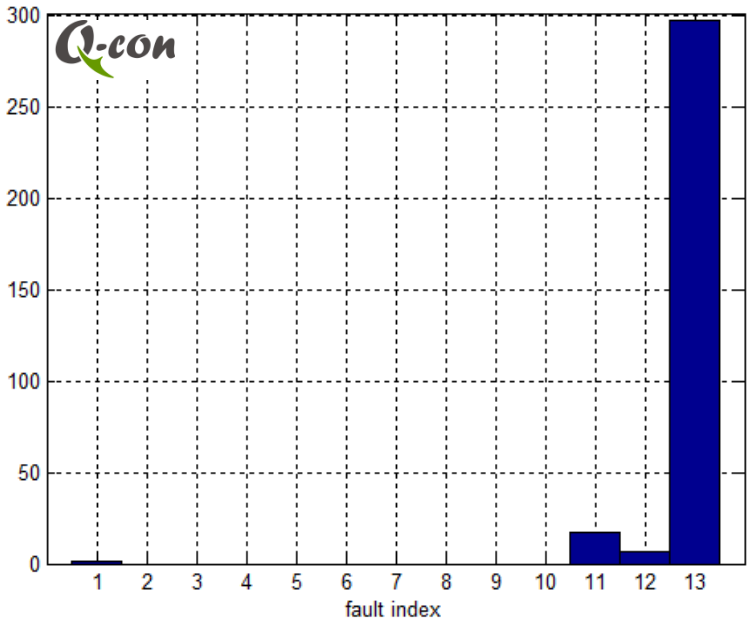

Figure 37: Histogram showing the number of events which were collapsed onto a certain fault in the minimum complexity model.

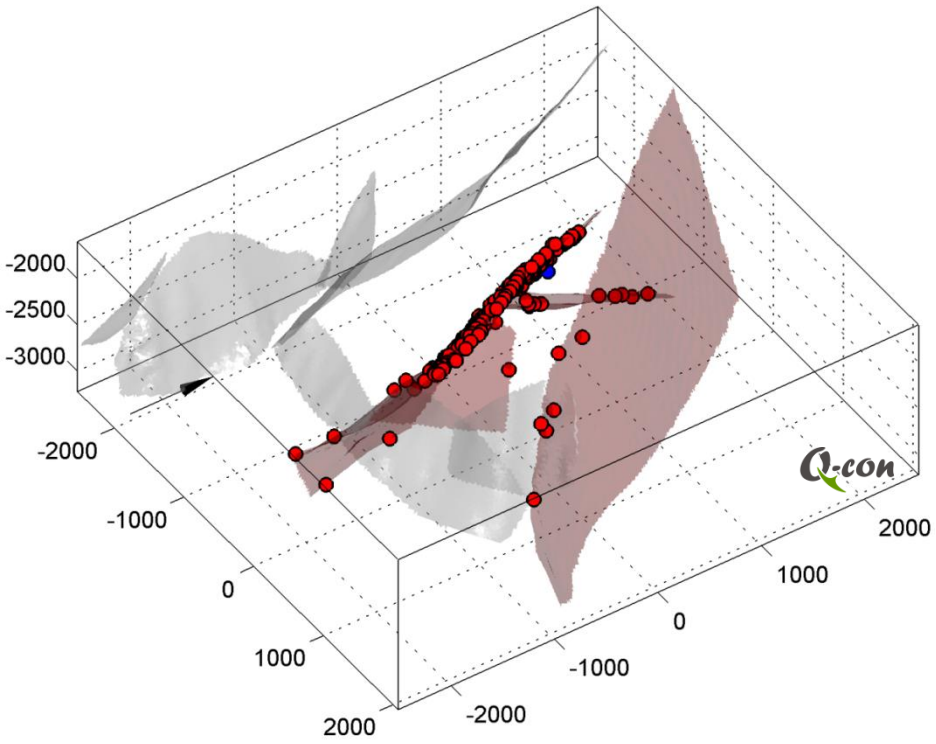

Figure 38: Fault-collapsed hypocenter locations in the minimum complexity model. Hypocenters that can be shifted onto a fault within their 2σ confidence limits (componentwise) show up in red. Four hypocenter solutions do not match a mapped fault within their confidence limits. Three of these have symmetric solutions and were discarded; the remaining event was assigned its original hypocenter (blue dot). Seismically active faults are denoted by red shading.

APPENDIX C MAXIMUM COMPLEXITY MODEL

For addressing seismic hazard aspects in a conservative sense, it is also useful to investigate which fault patches could have been seismically active given the observation data. Figure 39 shows this 'maximum fault complexity model' with the complete set of fault patches that could have been seismically active given the 2σ uncertainty limits of the hypocenter locations. Even in the maximum complexity model, seismicity is constrained to the reservoir faults and the immediate boundary faults.

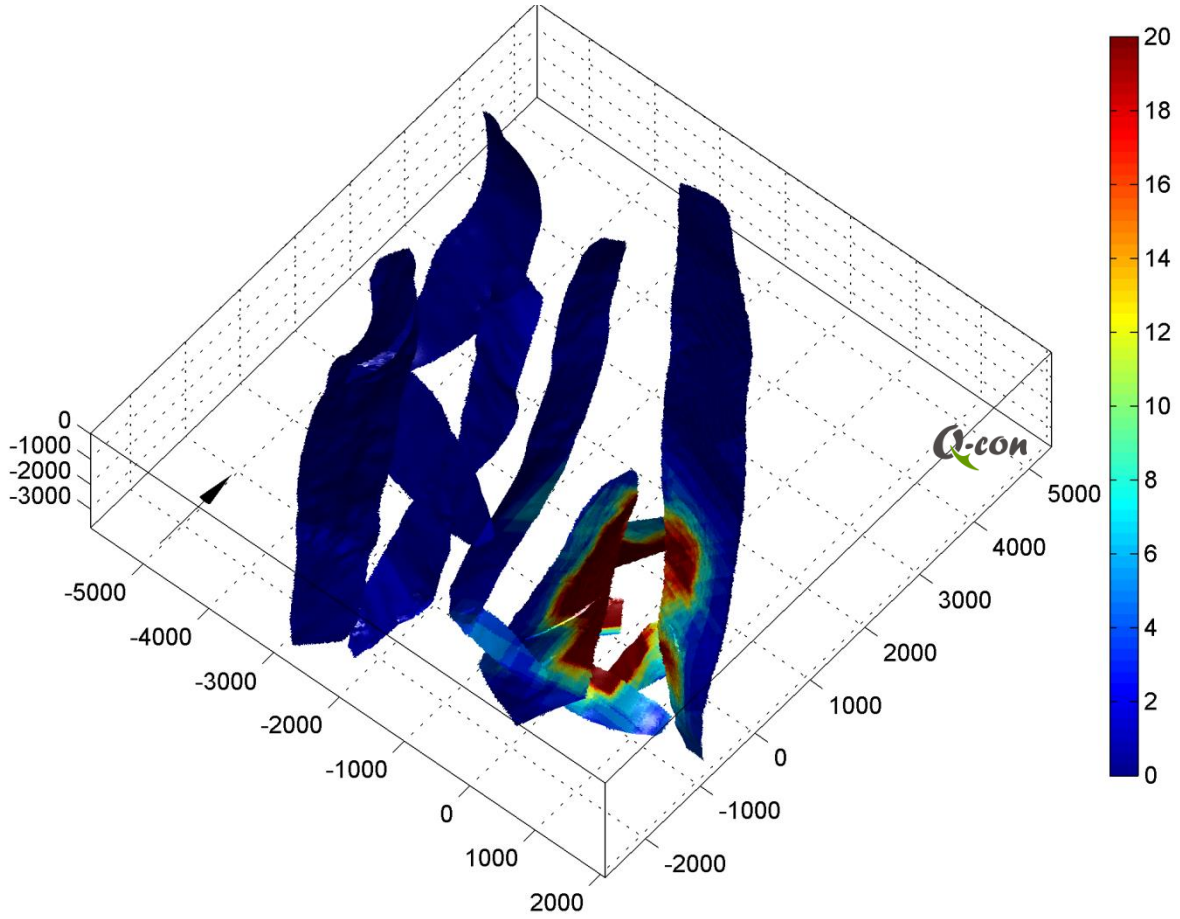

Figure 39: Seismic activity in the 'maximum fault complexity model'. Fault collapsing is applied to all reservoir events and all fault patches within the 2σ range (componentwise) of an individual event are counted. Color encoding denotes event counts on fault patches according to the colorbar. The colorbar is saturated at 20 counts for displaying purposes.

APPENDIX D EARTHQUAKE CATALOGUE

Processing results were stored in a data catalogue (160113_BGS_catalogue.xls) accompanying this report. For six events, the hypocenter inversion is not overdetermined resulting in infinite hypocenter location errors. These events were excluded from the seismicity interpretations.

column	comment
event id	event identifier; negative values denote 'symmetrical' hypocenter solutions
time	event occurrence time
M_w	Hanks & Kanamori (1979) moment magnitude
hypo x	hypocenter location, eastern direction
hypo y	hypocenter location, northern direction
hypo z	hypocenter location, vertical direction
dx	2σ total hypocenter location error, eastern direction
dy	2σ total hypocenter location error, northern direction
dz	2σ total hypocenter location error, vertical direction
fault hypo x	fault-collapsed hypocenter location, eastern direction
fault hypo y	fault-collapsed hypocenter location, northern direction
fault hypo z	fault-collapsed hypocenter location, vertical direction
orig hypo x	original hypocenter location, eastern direction
orig hypo y	original hypocenter location, northern direction
orig hypo z	original hypocenter location, vertical direction
orig mag	original catalogue magnitude
ME id	id of master-event used for relative hypocenter location
ME x	relative hypocenter location, eastern direction
ME y	relative hypocenter location, northern direction
ME z	relative hypocenter location, vertical direction

Table 11: Description of earthquake catalogue '160113_BGS_catalogue.xls'. All coordinates are stated in meters with respect to the wellhead of BGM3.

APPENDIX E FAULT MODEL

Index	Fault Name
1	BGM 11
2	BGMPDD-BBB-EAST-01
3	BGMPDD-BER-EAST-01
4	BGMPDD-BER-EAST-02
5	BGMPDD-BER-EAST-03
6	BGMPDD-BER-WEST-01
7	BGMPDD-BGM-SOUTH-01
8	BGMPDD-BGM-SOUTH-02
9	BGMPDD-BGM-WEST-01
10	BGMPDD-BLOCK1-02
11	BLOCK1A-1B
12	EAST
13	MID FIELD

Table 12: Fault index used in the current study and associated fault name in the FENIX model.